Fermi National Accelerator Laboratory

FERMILAB-Pub-91/23-E
[E-741/CDF]

Measurement of QCD Jet Broadening in $p\bar{p}$ Collisions at $\sqrt{s}$=1.8 TeV *

The CDF Collaboration
Fermi National Accelerator Laboratory
P.O. Box 500
Batavia, Illinois 60510

January 23, 1991

* Submitted to *Phys. Rev. D.*, January 23, 1991

FERMILAB-PUB-91/23-E
CDF/PUB/JET/PUBLIC/1209
January 23, 1991

Measurement of QCD Jet Broadening in $p\bar{p}$ Collisions at $\sqrt{s} = 1.8$ TeV

F.Abe[p], D.Amidei[c], G.Apollinari[k], G.Ascoli[g], M.Atac[d], P.Auchincloss[n], A.R.Baden[f], A. Barbaro-Galtieri[i], V.E.Barnes[l], F.Bedeschi[k], S. Behrends[l], S.Belforte[k], G.Bellettini[k], J.Bellinger[q], J.Bensinger[b], A.Beretvas[n], P.Berge[d], S.Bertolucci[e], S.Bhadra[g], M.Binkley[d], R.Blair[a], C.Blocker[b], J.Bofill[d], V.Bolognesi[k],A.W.Booth[d], G.Brandenburg[f], D.Brown[f], A.Byon[l], K. L. Byrum[q], M. Campbell[c], R.Carey[f], W.Carithers[i], D.Carlsmith[q], J.T.Carroll[d], R.Cashmore[d], F.Cervelli[k], K.Chadwick[d,l], T.Chapin[m], G.Chiarelli[k], W.Chinowsky[i], S.Cihangir[o], D.Cline[q], D.Connor[j], M. Contreras[b], J.Cooper[d], M.Cordelli[e], M.Curatolo[e], C.Day[d], R.DelFabbro[k], M.Dell'Orso[k], L.DeMortier[b], T.Devlin[n], D.DiBitonto[o], R. Diebold[a], F.Dittus[d], A.DiVirgilio[k], J.E.Elias[d], R.Ely[i], S.Errede[g], B.Esposito[e], A. Feldman[f], B.Flaugher[n], E.Focardi[k], G.W.Foster[d], M.Franklin[f,g], J.Freeman[d], H.Frisch[c], Y.Fukui[h], A.F.Garfinkel[l], P.Giannetti [k], N.Giokaris[m], P.Giromini[e], L.Gladney[j], M.Gold[i], K.Goulianos[m], C.Grosso-Pilcher[c], C.Haber[i], S.R.Hahn[j], R.Handler[q], R.M.Harris[i], J.Hauser[c], T.Hessing[o], R.Hollebeek[j], P.Hu[n], B.Hubbard[i], P.Hurst[g], J.Huth[d], H.Jensen[d], R.P.Johnson[d], U.Joshi[n], R.W.Kadel[d], T.Kamon[o], S.Kanda[p], D.A.Kardelis[g], I.Karliner[g], E.Kearns[f], R.Kephart[d], P.Kesten[b], H.Keutelian[g], S.Kim[p], L.Kirsch[b], K.Kondo[p], U. Kruse[g], S.E.Kuhlmann[l], A.T.Laasanen[l], W.Li[a], T.Liss[c], N.Lockyer[j], F.Marchetto[o], R.Markeloff[q], L. A. Markosky[q], P.McIntyre[o], A.Menzione[k], T.Meyer[o], S.Mikamo[h], M.Miller[j], T.Mimashi[p], S.Miscetti[e], M.Mishina[h], S.Miyashita[p], N.Mondal[q], S.Mori[p], Y.Morita[p], A.Mukherjee[d], C.Newman-Holmes[d], J. Ng[f], L.Nodulman[a], R.Paoletti[k], A.Para[d], J.Patrick[d], T.J.Phillips[f], H.Piekarz[b], R.Plunkett[m], L.Pondrom[q], J.Proudfoot[a], G.Punzi[k], D.Quarrie[d], K.Ragan[j], G.Redlinger[c], J.Rhoades[q], F.Rimondi[d], L.Ristori[k], T.Rohaly[j], A.Roodman[c], A.Sansoni[e], R.Sard[g], V.Scarpine[g], P.Schlabach[g], E.E.Schmidt[d], P.Schoessow[a], M.H.Schub[l], R.Schwitters[f], A.Scribano[k], S.Segler[d], M.Sekiguchi[p], P.Sestini[k], M.Shapiro[f], M.Sheaff[q], M.Shibata[p], M.Shochet[c], J.Siegrist[i], P.Sinervo[j], J.Skarha[q], D.A.Smith[g], F.D.Snider[c], R.St.Denis[f], A.Stefanini[k], Y.Takaiwa[p], K.Takikawa[p], D.Theriot[d], A.Tollestrup[d], G.Tonelli[k], W. Trischuk[f], Y.Tsay[c], F.Ukegawa[p], D.Underwood[a], R.Vidal[d], R.G.Wagner[a], R.L.Wagner[d], J.Walsh[j], T.Watts[n], R.Webb[o], T.Westhusing[g], S.White[m], A.Wicklund[a], H.H.Williams[j], T.Yamanouchi[d], A.Yamashita[p], K.Yasuoka[p], G.P.Yeh[d], J.Yoh[d], F.Zetti[k]

(The CDF Collaboration)

[a] Argonne National Laboratory- [b] Brandeis University- [c] University of Chicago
[d] Fermi National Accelerator Laboratory- [e] INFN, Laboratori Nazionali di Frascati, Italy
[f] Harvard University- [g] University of Illinois- [h] KEK, Japan
[i] Lawrence Berkeley Laboratory-[j] University of Pennsylvania
[k] INFN, University and Scuola Normale Superiore of Pisa, Italy- [l] Purdue University
[m] Rockefeller University- [n] Rutgers University- [o] Texas A&M University
[p] University of Tsukuba, Japan- [q] University of Wisconsin

Submitted to Phys. Rev. D, January 23, 1991

Abstract

A measurement of the QCD Jet Broadening parameter, $< Q_T >$, is described for high E_T jet data in the central CDF calorimeter. As an alternate approach to clustering analysis, this method involves the use of a global event parameter which is free from the ambiguities associated with the definition and separation of individual clusters. The parameter, Q_T, is defined as the scalar sum of the transverse momentum perpendicular to the transverse thrust axis. Parton level QCD predictions are made for $< Q_T >$ as a function of E_T, the total transverse energy in the events, and suggest that a measurement would show a dependence on the running of the strong coupling constant, α_s. Comparisons are made to first-order QCD parton level calculations, as well as to fully evolved and hadronized leading log simulations. The data are well described by the QCD predictions.

PACS numbers: 13.87.-a, 12.38Qk, 13.85.Ni

1 Introduction

The search for precise, unambiguous experimental tests of Quantum Chromodynamics (QCD) dates from the earliest observations of a jetlike structure in e^+e^- collisions.[1] In these first tests, performed at SLAC[1] and DESY[2], jetlike structure was identified through the use of event shape variables such as thrust and sphericity. In particular, the jet-like characteristics of the events were observed to increase with increasing center-of-mass energy (the range of 6.2-7.4 GeV was covered in Ref. 1). Models with two jet structure were shown to give better agreement with the data than phase space models for multihadron production.

The advent of higher center-of-mass energies made it possible to also discern a clear three jet component in hadronic final states.[3,4,5] These analyses also relied on global event measures, such as sphericity, thrust and oblateness. The comparison, however, to perturbative QCD predictions relied strongly on semi-empirical models which described the non-perturbative phase of hadronization. These comparisons demonstrated the mechanism of gluon bremsstrahlung in three jet production. In addition, the fraction of three jet events was taken as a measure of the strong coupling constant.[6,7,8] The experimentally derived values of α_s for these studies were found to be largely dependent on the choice of the scheme for fragmentation.

A further refinement in the use of global event variables in e^+e^- collisions was the introduction of the energy-energy correlation, which is less sensitive to the effects of fragmentation than the previously used variables.[9] Reviews of this technique, and experimental considerations can be found in Refs. 10 and 11.

The use of global measures has not been limited to e^+e^- collisions, however. Measurements of jet production in proton-proton and proton-antiproton collisions have used global event variables to identify and measure jet structure in hadronic final states at high transverse energies.[12,13]

In contrast to the global event measures, jet clustering algorithms were developed to associate groups of particles, or clusters of energy directly with partons.[14,15] The clustering technique has the advantage that as the jet energy increases, the identification of clusters with partons should become less ambiguous, allowing more direct comparisons with perturbative QCD. This approach has been pursued extensively in both proton-antiproton collisions and e^+e^- collisions. The association of the measured jet or cluster energy can be corrected back to the original parton energy via Monte

Carlo simulations in order to facilitate comparison with parton level QCD calculations.

Early analysis of CDF data has been based on clustering techniques, and has demonstrated that the inclusive jet cross-section[16] and angular distributions of di-jet events[17] are in good agreement with leading order ($O(\alpha_s^2)$) QCD predictions. An example of the jet structure observed in the CDF calorimeter is shown in Fig. 1.

Experimentally, when a clustering analysis is used, the sensitivity to final states containing more than two partons is limited to cases where radiated gluons can be identified as independent clusters. This imposes both energy and angular restrictions on the emitted gluon and reduces the sensitivity to low energy and collinear gluon emission. For example, the CDF clustering algorithm has a characteristic size of ≈ 0.7 radians and a minimum cluster energy cut that corresponds roughly to a 20 GeV parton. The event in Fig. 1 could be designated as either a two-jet or three-jet event, depending on the cluster definition. In this case, global event measures have the advantage that the sensitivity to clustering parameters is removed.

In this paper, we discuss the use of an event shape parameter, Q_T, introduced by R. K. Ellis and B. Webber to describe hadronic final states in proton-antiproton collisions.[18] Q_T is defined as the scalar sum of the momenta perpendicular to the transverse thrust axis, where the transverse thrust axis represents the direction of maximum energy flow in the plane transverse to the beam. It has the property of being both finite and calculable for all multiparton final state configurations, particularly the case where singularities occur in perturbation theory associated with the collinear emission of gluons. This is to be contrasted to other variables, such as sphericity, which are not well behaved in this limit. This is also in contrast to clustering analyses, where cut-offs are imposed in both the theory and experiment to avoid the regions where the

perturbative results diverge and independent clusters can not be resolved. The behavior of Q_T with increasing energy is termed jet broadening because of its sensitivity to the increasing multiparton nature of a jet as the energy of the jet increases.

While the perturbative QCD calculations presented by Ellis and Webber are based on a parton level description of the events, hadrons, not partons, are measured in a detector and both hadronization and gluon emission will effect the shape (broadness) of the resulting cluster of particles. If gluon emission did not contribute to the size of a jet, then the angular spread of the jet of hadrons would decrease roughly linearly with increasing energy of the parton.[19] Because of gluon emission, the size of a jet transverse to a central axis will not decrease linearly, but more slowly (e.g. logarithmically) with energy.

The behavior of Q_T over the energy range spanned by the CDF data is, in principle, sensitive to the logarithmic evolution of the strong coupling constant, α_s . Comparison of perturbative QCD predictions for Q_T to CDF data provides a new test of QCD for the highest energy hadron collisions available with sensitivity to order $O(\alpha_s^3)$ processes without the angular separation and energy cuts associated with a clustering type of analysis.

In Section 2, the theoretical definition of Q_T is described. Presented in section 3 are the elements of the detector and trigger system pertinent to this analysis; Section 4 describes the data sample and analysis. Comparisons to the theoretical predictions will be presented in Section 5. Section 6 contains a summary of our conclusions.

2 Theoretical Definition of Q_T

To avoid complications due to boosts, the parameters used here are defined in the transverse plane, e.g. $E_T = Esin\theta$, where θ is the angle between the particle and the beamline. The total transverse energy of an event, E_T, is defined to be the sum of the transverse energies of all partons falling inside some fixed, symmetric rapidity interval. The transverse thrust axis, $\vec{n_t}$, is defined as the axis in the plane perpendicular to the beamline having the maximum transverse energy flow:

$$T_t = MAX \sum_{i=1}^{n} \frac{|\vec{E_T^i} \bullet \vec{n_t}|}{E_T},$$

where T_t is the transverse thrust, and $\vec{E_T^i}$ is the projection of the parton momentum vector onto the transverse plane. Q_T is defined as the scalar sum of the parton momenta perpendicular to the transverse thrust axis:

$$Q_T = \sum_{i=1}^{n} |\vec{E_T^i} \times \vec{n_t}|.$$

An important feature of this definition is that Q_T is identically zero for a 2⇒2 parton event. Hence Q_T is infrared safe, meaning that it goes to zero in the limit that the energy of an emitted gluon approaches zero. It should also be noted that Q_T does not change if one or more of the partons are split into collinear partons.

The simplest nonzero configuration for Q_T is for a three parton final state. The tree-level expression for Q_T in the process $1 + 2 \Rightarrow a + b + c$ has been written by Ellis and Webber[18] as:

$$< Q_T > \frac{d\sigma}{dE_T} = \frac{E_T^4}{512\pi^4 s^2} \int dy_a dy_b dy_c dz_a dz_b \frac{f_A(x_1)}{x_1} \frac{f_B(x_2)}{x_2} \frac{z_a z_b z_c}{Z_t} \sum < |M^{12 \to abc}|^2 >, \quad (1)$$

where the invariant mass of the colliding $p\bar{p}$ pair is $\sqrt{s}$, y_i is the rapidity of outgoing parton i, $z_i = E_T^i/(\frac{E_T}{2})$ and $Z_t = MAX(z_i)$. The structure functions $f_A(x_1)$ and

$f_B(x_2)$ correspond to parton 1 in proton A and parton 2 in antiproton B. Since Q_T is infrared-safe and stable against the collinear singularity, it is possible to evaluate this expression without any restrictions on the minimum E_T^i of the partons or any requirement on the angular separation between the partons.

The results presented here will be in terms of the mean Q_T found in a given bin of E_T. Operationally, $< Q_T >$ is determined in separate intervals of E_t. To calculate $< Q_T >$, the integral of Q_T is determined for each E_T interval from Eq. 1. Because of the divergences in the tree-level $2 \Rightarrow 3$ matrix elements, the $2 \Rightarrow 2$ parton process is used to normalize the calculation in any given interval of E_T. For the case where partons 1 and 2 collide and produce partons a and b, this can be written[18] as:

$$\frac{d\sigma}{dE_T} = \frac{E_T}{32\pi s^2} \int dy_a dy_b \frac{f_A(x_1)}{x_1} \frac{f_B(x_2)}{x_2} \sum < |M^{12\to ab}|^2 > . \qquad (2)$$

The mean value, $< Q_T >$, thus obtained produces the leading order estimate of the $< Q_T >$ in each bin of E_T.

Figure 2 shows $< Q_T >$ as a function of E_T. The Q^2 scale was chosen to be E_T^2 for the event. The structure functions were Duke and Owens set 1,[20] and the one loop leading logarithm approximation was used for the evolution of α_s. These calculations were performed with the restriction that all of the partons lie within the central pseudorapidity region, $-1.1 \leq \eta_i \leq +1.1$, which corresponds to the coverage of the central CDF detector.

It is important to note that, although there is a kinematic limit to the maximum value of Q_T for an event with a given E_T, the theoretical calculation of $< Q_T >$ need not respect the limit. The sum-Q_T (Eq. 1) is normalized by the number of events from a separate calculation (Eq. 2) and nothing explicitly relates these two independent integrations. For a three-parton final state, the kinematic limit on Q_T/E_T is 0.58, and

for arbitrary final states it is 0.71.[18] As discussed in Ref. 18, the level at which the calculation respects the kinematic bounds is an indication of its validity in this region of E_T.

As shown in Fig. 2, $< Q_T >$ rises as the E_T of the events increases. This jet broadening is, in part, due to the fact that Q_T is strongly correlated with the E_T in an event. Alternatively, the behavior of the dimensionless quantity $< Q_T > /E_T$ is a measure of the relative amount of Jet Broadening as a function of E_T. As the ratio of an order α_s^3 calculation to an order α_s^2 calculation, $< Q_T > /E_T$ should be roughly linear in α_s. This quantity is similar to the ratio of the cross sections of three-jet to two-jet events in terms of the uncertainty of the contributions of higher order terms, but it is free from the ambiguities (theoretical and experimental) associated with the definition and separation of three and two-jet events.

To investigate the sensitivity of this quantity to the running of α_s, the calculation was performed for a fixed value of α_s. Figure 3 shows a comparison of the $< Q_T > /E_T$ curves with and without α_s running. The constant used for α_s was chosen at the lowest point on the curve, $Q^2 = E_T^2 = (50\ \text{GeV})^2$, $\alpha_s = 0.134$. The curve without α_s running shows much less energy dependence than if α_s is allowed to run. Also shown in Fig. 3, is the $< Q_T > /E_T$ curve where the structure function evolution is fixed at $Q^2 = E_T^2 = (50\ \text{GeV})^2$. This curve indicates that the behavior of the ratio $< Q_T > /E_T$ with E_T is related to the running of the coupling constant and is relatively insensitive to the evolution of the structure functions.

The sensitivity of $< Q_T > /E_T$ to the choice of structure functions and Q^2 scale was investigated by performing four separate calculations: $< Q_T > /E_T$ as a function of E_T was evaluated using Duke and Owens structure function sets 1 and 2 with the Q^2

scale set to E_T^2 and $E_T^2/4$. Figure 4 shows that a change in the Q^2 scale results in a shift in the overall level of $< Q_T > /E_T$, although the shape of the curve remains the same. These two sets of structure functions use Λ's that differ by a factor of 2, and thus, if both sets are evaluated with the same Q^2 scale, the α_s used in these calculations is different. By choosing the Q^2 scale of $E_T^2/4$ for set 1, and $Q^2 = E_T^2$ for set 2, the same value of α_s is achieved. The agreement between the curves for these choices indicates that while the level of $< Q_T > /E_T$ is sensitive to the choice of scale, the shape of the $< Q_T > /E_T$ curve comes mainly from the running of the strong coupling constant and is not sensitive to the choice of structure functions.

In the calculations discussed above, all of the partons were restricted to fall within the central rapidity region, while in the experiment one or more of the partons may fall outside this region. To study this effect, events were generated with less stringent requirements on the parton rapidities and then $< Q_T > /E_T$ was calculated using only those partons that fall within the central region. For this study, the QCD Monte Carlo program PAPAGENO[21] version 3.09 was used.

The PAPAGENO program evaluates one specific process at a time, i.e. it will perform either the $2 \Rightarrow 2$ or the $2 \Rightarrow 3$ calculation. When the PAPAGENO program evaluates the $2 \Rightarrow 3$ process, cuts on angular separation and minimum P_T are typically imposed to avoid divergences in the three-jet matrix elements. To simulate the Ellis and Webber calculations a slight modification of the program was necessary.[22] In effect, the fact that $Q_T \rightarrow 0$ as the $2 \Rightarrow 3$ matrix element diverges was used to balance that region of the calculation. Figure 5 shows the Ellis and Webber calculation compared to the PAPAGENO results for the case where all the partons are generated within a maximum rapidity of ± 1.1. Both PAPAGENO and the Ellis and Webber calculations

shown in the figure were performed with Duke and Owens structure functions set 1, with $Q^2 = E_T^2$ and the same one loop approximation for α_s .

Also shown in Fig. 5 are the $< Q_T > /E_T$ curves from PAPAGENO for the case where the partons are generated with larger rapidity ranges. Although the events are generated with various rapidity cuts, the $< Q_T > /E_T$ calculation is performed using only those partons that fall within the central rapidity region. These results show that beyond a rapidity of 2.5, the $< Q_T > /E_T$ curve is insensitive to the rapidity region used to generate the events and that events which are not completely contained in the central region make a significant contribution to $< Q_T > /E_T$ in the low E_T region.

With the PAPAGENO program it is also possible to set the value of the α_s to a constant. Figure 6 shows the $< Q_T > /E_T$ curves for a generated rapidity range of 4.0 with and without α_s running. The shapes of the curves are now similar, although there is a shift in the overall level of $< Q_T > /E_T$. While these results indicate only minimal sensitivity to the running of α_s, a measurement of $< Q_T > /E_T$ provides a test of order $O(\alpha_s^3)$ QCD predictions.

For these calculations, the effects of hadronization and the underlying event have not been considered. These effects will be discussed in Section 5 when the data are compared to QCD predictions.

3 Apparatus

CDF is a multi-detector system with complete 2π azimuthal coverage as well as large coverage in pseudorapidity (maximum range of $-4.2 \leq \eta \leq 4.2$). A schematic of the CDF detector is shown in Fig. 7. The central detector consisted of charged particle tracking chambers located inside a solenoidal magnet surrounded by electromagnetic and hadronic calorimeters, muon detection chambers and a steel yoke. Symmetric forward and backward systems included electromagnetic and hadronic calorimeters, iron toroids, and muon chambers. As all the components of the CDF detector have been described in detail elsewhere,[23] only the components used in this analysis will be discussed further. The right-handed coordinate system used here has its z-axis along the proton beam with the origin at the vertical symmetry plane of the detector (the nominal collision point). The y-axis is vertically upward. We also use the azimuthal angle, ϕ, and the polar angle, θ. The pseudorapidity is $\eta = -ln[tan(\theta/2)]$.

3.1 Tracking

For each event, the interaction vertex was located with the Vertex Time Projection Chamber (VTPC).[24] Surrounding the VTPC, but also within the 1.5 Tesla solenoidal field, the Central Tracking Chamber (CTC)[25] provided high resolution momentum information about charged particles. The CTC covered the angular region $40° \leq \theta \leq 140°$ and has track momentum resolution $\delta P_t/P_t^2 \leq 0.002$ (GeV/c)$^{-1}$.

3.2 Central Calorimeters

The CDF central calorimeters were constructed in a projective tower geometry, as shown in Figure 8. Each "tower" covered $\approx$0.1 units of pseudorapidity and 15° in azimuthal angle ϕ ; this segmentation was small enough that a typical jet was spread over multiple towers. Each half of the central detector was divided into 24 wedge shaped modules that were arranged in a barrel around the solenoidal coil and provided nearly complete 2π azimuthal coverage. A calorimeter tower consisted of an electromagnetic shower detector[26] in front of a hadronic calorimeter.[27]

The electromagnetic and hadronic components of a tower were each read out by two phototubes located on opposite sides of the tower in ϕ. From the balance of energy in the phototubes, the azimuthal location of the electromagnetic and hadronic showers within each tower was determined.

The average energy resolution of the calorimeters was determined from test beam data. The electromagnetic calorimeter[26] had a resolution of $\sigma(E)/E = 13.5\%/\sqrt{E sin\theta}$. For 50 GeV pions, the average energy resolutions of the hadronic calorimeters were 11% for the central and 14% for the end-wall detectors.[23] The hadron calorimeters were equipped with Time to Digital Converters (TDC's) which were used to determine the arrival time of signals. As described in section 4.2, the hadron TDC timing information was used to reject backgrounds associated with cosmic rays and noise from the main ring accelerator.

The hadronic calorimeters were found to have nonlinear response, particularly for particles with energy below 10 GeV. No calorimeter test beam data was avaliable for particles in this energy range, but by using the central tracking information in the minimum-bias data sample, the average response of the central calorimeter for isolated

low momentum tracks was measured. The measurements apply to charged particles with P_T above 0.4 GeV. Below this P_T threshold charged particles curl in the 1.5 Tesla magnetic field and never reach the calorimeter face. The procedure involved summing the energy in a 3×3 block of towers (to include the effects of shower spreading) and making strict isolation requirements to minimize contributions from other particles. Figure 9 shows the average response of the central calorimeter, electromagnetic+hadronic, to charged particles below 10 GeV together with test beam results for particles above 10 GeV.

The results shown in Fig. 9 were used to make an average correction for the nonlinear calorimeter response. The correction was performed by taking all tracks in each event, projecting each track through the magnetic field to the face of the calorimeter and then correcting the struck tower for the difference between the original track momentum and the average calorimeter response to a particle of that momentum. An upper limit on the track P_T of 100 GeV was applied since, at high energy, the calorimeter resolution is better than the tracking resolution. Additional corrections for low energy neutral particles and other detector effects will be discussed in section 4.

3.3 Beam-Beam Counters

The Beam-Beam Counters[28] consisted of two planes of scintillating plastic located in front and in back of the central calorimeters. Each plane of counters covered the angular region $0.32° \leq \theta \leq 4.47°$. A coincidence of hits in both the forward and backward counters was used to define the minimum-bias trigger. This requirement was used in conjunction with other trigger requirements to reduce the contribution of beam gas collisions, which typically have all the particles moving either in the forward

or backward direction, but not both.

The Beam-Beam counters also provided a monitor of the luminosity. This was accomplished by recording a constant fraction of events which were required to satisfy only the minimum-bias trigger. A Monte Carlo study and extrapolation from lower energies indicated that the total cross section for events in the angular region covered by the Beam-Beam counters was 44 ± 6 mb.[16] This, combined with the number of events in the minimum bias data sample, determined the absolute scale of the luminosity measurement.

3.4 Trigger

The data sample was collected in 1987 with the requirement of a "minimum-bias" trigger in coincidence with calorimeter E_T deposit above an adjustable threshold. The calorimeter trigger used trigger towers which covered $\approx$0.2 units of pseudorapidity by 15° in ϕ. In the central region two detector towers ganged together in η comprise one trigger tower. The transverse energy of a trigger tower was calculated assuming an event vertex at z = 0. The E_T summation included all trigger towers in the central calorimeter that had more than 1 GeV transverse energy in either the electromagnetic, hadronic or in the sum of the electromagnetic and hadronic components of the tower. The E_T summation also included towers above threshold in the plug and forward electromagnetic calorimeters. Due to noise problems in the hadronic calorimeters in the plug and forward regions, energy in these detectors was excluded from the sum.

To keep the deadtime to a tolerable level over the wide range of luminosities, the E_T threshold on the trigger was varied. The E_T thresholds, trigger names and the corresponding integrated luminosity at each threshold are shown in Table 1. The

numbers in the table represent the integrated luminosity used in this analysis and have a total integrated luminosity of 23.6 nb^{-1}.

4 Offline Analysis

4.1 Measurement of Global Event Parameters

Calculation of global event parameters from the raw data was accomplished by using the finely segmented calorimeter structure of the CDF detector. Conceptually, the energy of each tower was treated as if it were the energy of a particle. The location of the energy within the detector was used to determine the components of the "particle" momentum vector in the coordinate system where the origin is at the z location of the event vertex. The transverse energy of tower i, E_T^i, is the sum of the transverse energy in the electromagnetic and hadronic components of that tower:

$$E_T^i = E_{em}^i sin\theta_{em}^i + E_{had}^i sin\theta_{had}^i.$$

A single ϕ position for the tower energy was determined using the E_T weighted mean of the ϕ centroid positions in the electromagnetic and hadronic components. The x and y components of the "energy" associated with tower i were calculated as:

$$E_x^i = E_T^i cos\phi^i,$$

$$E_y^i = E_T^i sin\phi^i.$$

As the calorimeter measured energy, not momentum of particles, and each calorimeter tower was treated as a zero mass particle, and the components of "particle" transverse momentum were written as E_x^i, and E_y^i. The E_T of an event was defined as:

$$E_T = \sum_{i=1}^{n} E_T^i,$$

where n was the number of towers above threshold. The effect of the tower threshold cut will be discussed later. Figure 10 shows the uncorrected E_T spectrum for the

different trigger samples. The data has been normalized by the relative luminosities of the different samples. For this analysis, the sum was limited to the central rapidity region of $-1.1 < \eta < 1.1$ and to towers with $E_T^i > 0.2$ GeV.

Once the E_T^i and ϕ^i of each tower was calculated, the transverse thrust axis was determined from the energy flow in the events. The thrust was calculated using an iterative algorithm which began with the locations of the four highest energy particles (towers) in the event. Iterations continued until the convergence limit for the value of the thrust was reached in two successive iterations.

Figure 11 shows the angular distribution of the transverse energy flow with respect to the transverse thrust axis for a sample of events from the 30 GeV trigger. The horizontal axis represents the angle $\Delta\phi^i$ between the towers in the event and the thrust axis. The vertical axis represents the transverse energy of the towers. Each tower in each event is entered in this plot, and the plot represents the sum over this data sample. The spikes at 0° and 180° correspond to the presence of two jet activity in the events.

Calculation of Q_T from the data was accomplished by using the angle $\Delta\phi^i$ between each tower and the thrust axis:

$$Q_T = \sum_i^n |E_T^i sin\Delta\phi^i|.$$

To mimic the theoretical calculations, $< Q_T > /E_T$ was constructed from the data as follows: a two-dimensional histogram of Q_T versus E_T was filled and $< Q_T >$ was calculated in 20 GeV slices of E_T; then the mean Q_T in that slice was divided by the mean E_T in that slice. Figure 12 shows the raw Q_T distributions in the 20 GeV slices of E_T .

4.2 Background removal

Before calculating the $< Q_T > / E_T$ curve from the raw data, the obvious backgrounds were removed. In some cases, energy within a given event could be identified as fake, i.e. not associated with the particles from the collision, and this energy could be suppressed. In other cases, entire events were rejected as background. The methods and algorithms developed for identifying fake energy, and for identifying background events are discussed below.

One of the largest sources of false energy was random discharges from the central phototubes. Since the energy in each tower is independently measured by two phototubes, these discharges could be identified by checking the energy ratio between the phototubes. If the balance of energy between the tubes was outside reasonable limits, the high energy tube was assumed to be from a fake discharge and the measurement from the other tube was used to determine the energy. If the energy from one tube was suppressed, the ϕ location of the remaining energy was taken as the center of the tower.

There were two sources of background events in the raw data: accelerator-induced energy and cosmic rays. The main ring is a synchroton composed of conventional magnets which passes directly above the CDF detector. During normal data taking it was used for the production of antiprotons. Losses associated with the main ring beam would sometimes deposit large amounts of energy in the top portion of the hadron calorimeters. This was termed "main ring splash". Removal of these events offline was accomplished by using information from the TDCs on the hadron calorimeter. An algorithm was developed which summed the energy deposited outside a timing window around the beam crossing. The specific cuts rejected events with more than 8 GeV of

energy outside the 35 ns timing window. These time-of-flight cuts were also efficient against cosmic ray muons that emit bremsstrahlung photons in the hadron calorimeters. At high E_T , the background was roughly constant with E_T . The parameters of this algorithm were tuned such that the cuts rejected no events that could have come from real $p\bar{p}$ collisions and left negligible background at low E_T .

Backgrounds that remained included in-time cosmic rays and cosmic rays that emit photons in the electromagnetic calorimeters (which do not have TDC's). Tracking information was used to eliminate such events. Events without tracks ($\approx 1\%$) were excluded from the sample. Finally, all 102 of the events with E_T above 200 GeV were visually scanned and 2 cosmic ray background events were identified and removed.

The depositions of energy described above resulted in some events that passed the trigger requirements (Table 1) only because of fake energy. Also, since the trigger included the plug and forward electromagnetic calorimeters, the raw event sample contained events which passed the trigger threshold because of energy in those detectors. To remove these events, a software program, which simulated the trigger, was run on the data after the noise and background removal were performed. Events which did not pass the trigger sum E_T cut using only the energy in the central region were rejected.

4.3 Trigger bias and single tower threshold

As shown in Table 1 and Fig. 10, four trigger thresholds were used for data collection. These separate samples were combined, as discussed below, in order to maximize the range of E_T over which $< Q_T >$ was measured.

In determining the total E_T and Q_T of an event, a crucial variable is the tower threshold E^i_{Tmin}. When the central E_T was calculated by the trigger hardware, an

E^i_{Tmin} of 1.0 GeV was applied to each "trigger tower". To minimize corrections based on the Monte Carlo modeling of the low energy single particle spectra, a low single tower threshold E^i_{Tmin} of 0.2 GeV was chosen for the offline analysis. It is important to note that the single tower threshold affects the mixture of soft broad (high Q_T) events and hard collimated (low Q_T) events at a given E_T. The original mixture in the data was determined by the trigger, and thus when a lower single tower threshold is applied to detector towers, the soft events pick up more additional E_T (and Q_T) than the highly collimated di-jet events. As shown in Figure 10, the turnover in the raw E_T spectrum is higher than the trigger threshold due to the lower single tower threshold used in the calculation of the raw event E_T.

Figure 13 shows the $< Q_T > /E_T$ distributions for the separate trigger samples after the nonlinearity corrections have been performed. The turnover in the $< Q_T > /E_T$ curves shows the depletion of high Q_T events due to the stiff single tower threshold used in the trigger. Above the turnover in the curves the trigger reaches full efficiency. Based on the overlap of the separate trigger samples in these plots, cuts on track-corrected E_T were derived to produce a sample which was free from the bias associated with the trigger. No overlap was possible for the SUM-ET-20 sample however, so a conservative cut above the turn-over of the $< Q_T > /E_T$ curve was made. These cuts are shown in Table 2.

The distribution of $< Q_T > /E_T$ vs. E_T for the merged trigger samples is shown in Fig. 14. The errors on the points represent the statistical uncertainty in determining the mean Q_T in each E_T bin.

To find the uncertainty in the nonlinearity correction, the nonlinear response function was varied to its upper and lower limits. The corresponding shift in the corrected

$< Q_T > /E_T$ versus E_T provided a direct measure of the sensitivity of $< Q_T > /E_T$ to the uncertainty in this correction. The solid lines in Fig. 14 show the range around the $< Q_T > /E_T$ curve which results from uncertainty in the nonlinear response.

The other significant systematic uncertainty in data came from a shift in the noise level in the calorimeter electronics (pedestals) that occurred over the period of the data collection. Although, daily adjustments were made to correct such shifts, an asymmetric correction circuit allowed the channels to drift low without being corrected. Since the measurement of $< Q_T > /E_T$ is sensitive to the low energy response of the calorimeter, this drift created an additional uncertainty. The dashed curves in Fig. 14 show the range of uncertainty in $< Q_T > /E_T$ from the shifts. The uncertainty is asymmetric because of the asymmetry in the noise-level drift.

4.4 Corrections based on Detector Simulation

In addition to the corrections described above, it is also necessary to correct for effects such as detector resolution, energy losses in cracks, and energy lost below the single tower threshold. These effects were studied with an event generator (ISAJET[29]) and the CDF detector simulation.

Partons produced by the generator (ISAJET) are fragmented independently (Field-Feynman approach) and then the short-lived particles decay. (Note that fragmentation here means the conversion of the fully evolved ISAJET partons into hadrons.) The parameters used in the fragmentation functions were tuned to give good agreement with the CDF jet data.[16] In addition to the hard parton collision, an underlying event was generated by ISAJET and simulated along with the hard collision products. The resulting hadrons, electrons, neutrinos and other particles were projected through the

magnetic field to the face of the calorimeter. From the locations, momenta, and directions of these particles after they have passed through the magnetic field, 'particle level' event parameters were determined. Particles that never reach the calorimeter (charged particles of P_T below 0.4 GeV curl-up in the magnetic field) and particles such as neutrinos, that deposit no energy in the detector, are also included. These 'particle level' event parameters represent the goal of the detector corrections.

The resolution of the detector, combined with the steeply falling E_T spectrum, determine the number of events that will fluctuate up to higher E_T bins from low E_T; this is termed resolution smearing. To account for this effect, a sample of events, jets plus underlying event, was generated and simulated with a falling E_T spectrum which reproduces that data well. After the generated events were passed through the detector simulation, the same single tower threshold, $E_T^i \geq 0.2$ GeV, was applied, and the same type of nonlinearity corrections were performed as for the data. Note that for any choice of single tower threshold, the detector corrections will be affected by how much energy is lost below the single tower threshold and how much is lost to particles that curl in the magnetic field. The use of the charged tracking information and low single tower threshold minimize the reliance on the Monte Carlo single particle P_T spectra.

The detector corrections were derived for both E_T and $< Q_T > /E_T$ since the detector properties can have different effects on these quantities (i.e. the low energy particles which dominate at wide angles from the jets may be influenced by the single tower threshold more than the particles along the jet axis). Correction factors for E_T were derived by comparing the simulated and track-corrected E_T to the "particle-level" E_T. The mean E_T correction factor as a function of track-corrected E_T is shown in Fig. 15a.

Corrections for $< Q_T > /E_T$ were derived in a similar manner. The energy dependence of the Q_T/E_T correction was accounted for by measuring the correction factors in three slices of track corrected E_T which spanned the range of the data. Figure 15b shows the Q_T/E_T correction factors for slices of track-corrected E_T of 50-80 GeV, 100-140 GeV and 180-220 GeV. Interpolation between the curves based on the track-corrected E_T determined the Q_T/E_T correction factor at any intermediate E_T . The detector corrected $< Q_T > /E_T$ curve was formed by applying the correction factors event by event based on the measured track-corrected E_T and Q_T/E_T in each event. As a check for self-consistency, the detector corrections were applied to the simulated, track-corrected sample; good agreement was found between the fully detector corrected $< Q_T > /E_T$ curve and the $< Q_T > /E_T$ curve from the particle level.

The uncertainty in the detector correction factors was estimated using the detector simulation[30] and was combined in quadrature with the uncertainty associated with the nonlinear response and the pedestals. Figure 16 shows the fully detector corrected $< Q_T > /E_T$ curve where the solid lines represent the size of the systematic uncertainty in this result.

4.5 Underlying Event

The typical model for high E_T QCD events is a hard collision plus an underlying event associated with the spectator partons. The simplest model for the underlying event is an isotropic distribution of energy in $\eta - \phi$ space of the central detector, with an energy density independent of the total E_T in the event. This is the model we adopted. In this model, the energy from the underlying event is uncorrelated with the hard process and, averaged over many events, is uniformly distributed.

We chose to measure the underlying event energy density in our data, rather than to use Monte Carlo models to calculate it. We measured it in dijet events at angles near perpendicular to the thrust axis. This measurement must be corrected for apparatus effects in a manner nearly identical to that descibed above for the main event sample. Our procedure is as follows:

1. Apply dijet cuts to the data sample and histogram the uncorrected energy per unit angle with respect to the thrust axis as shown in Fig. 17. For this study, dijet events are defined as those with two hard clusters, each with $E_T \geq 20$ GeV.
2. Measure the average uncorrected energy density in the 20° interval around the perpendiculars to the thrust axis indicated by the arrows in Figure 17. This energy was summed over the entire pseudorapidity of the central detector ($-1.1 < \eta < 1.1$).
3. Generate an ISAJET Monte Carlo sample of events containing hard collisions and underlying event. Process these events through the detector simulation, reconstruct the events and subject them to the same dijet cuts as above.
4. Measure the *uncorrected* energy density in the MC sample as above.
5. Apply track corrections and detector corrections to the MC sample.
6. Measure the *corrected* energy density in the MC sample as above.
7. The ratio of corrected to uncorrected energy density in the MC sample was calculated to be 1.48.
8. The energy density measured from the real data was multiplied by this ratio to yield the corrected event energy density of 1.36 GeV/unit-rapidity/radian.
9. The fraction of this energy density arising from the underlying event was assumed

to be 75% (see discussion below), yielding a final underlying event energy density of 1.02 GeV/unit-rapidity/radian.

This procedure is described in detail in Ref. 30. The magnitude of this energy density is a measurement based on real data. The Monte Carlo sample and detector simulation were used only to determine the correction factor for detector effects in the same manner as for the main data sample. Although the magnitude of energy density determined by the Monte Carlo procedure was not used directly, it agreed with the measured energy density within ~30% which is within the systematic uncertainty assigned to this correction.

A number of studies were made to determine systematic uncertainties.

- In addition to requiring two hard clusters, other cuts for selecting di-jet events were investigated. The inability to distinguish high fluctuations in the underlying event from clusters associated with the hard scattering (i.e. multijet events), made the choice of di-jet cuts somewhat ambiguous. By taking a systematic uncertainty of 27% on the E_T density, the range of densities resulting from varying the cuts was covered.
- The dependence of the off-axis E_T density on the E_T of the clusters in the event was also studied. As shown in Fig. 18, no significant dependence on average cluster energy was observed.
- In principle, some of the energy belonging to the jets may have contributed to the off-axis energy bands. In order to estimate the size of this effect a second analysis was performed on a data sample that had one central cluster ($|\eta| \leq 1.1$) and one noncentral cluster ($|\eta| \geq 2.0$). The "central-central" sample had two jets which could contribute to the "off-axis" band whereas the "central-noncentral" sample

had only one. The central-plug sample was found to agree within statistical uncertainty with the central-central sample.

- There are uncertainties in the detector correction factor similar to those discussed in the previous subsection and shown in Fig. 16.
- The above items contribute to the measurement uncertainty. There is also a theoretical uncertainty. While the central-noncentral study indicated that there was no discernable contribution from the two leading jets at 90° from the thrust axis, Monte Carlo studies suggest otherwise. In particular, estimates using the HERWIG Monte Carlo indicated that 50% of the energy in the bands may come from the parton level scattering and shower evolution.[31,22] To cover the difference between this and what we infer from the data, the underlying event was assumed to contribute 75% of the energy observed in the bands, and an additional theoretical uncertainty of 25% was included.

The measurement uncertainties from the above sources were combined in quadrature and gave a total measurement uncertainty of 35% on the underlying event E_T density. The detector corrected underlying event E_T density is $1.02 \pm 0.35(meas.) \pm 0.25(theor.)$ GeV/unit-rapidity/radian.[30]

The average contribution of the underlying event to E_T and Q_T was derived by assuming an isotropic distribution of energy in the central detector. To find the contribution to $< Q_T >$, the average energy deposited in a 15° slice (corresponding to the ϕ segmentation of the calorimeter) was calculated from the energy density. The Q_T for this isotropic E_T distribution was then calculated by summing over each calorimeter slice and the angle from a given axis. The total E_T of the underlying event was found by summing over all towers in the central calorimeter. This resulted in an average

contribution to E_T of (14.1 $\pm$ 8.3) GeV and the average contribution to Q_T of (9.0 $\pm$ 5.3) GeV.

Finally, correcting the $< Q_T > / E_T$ curve involves subtracting the underlying event $< Q_T >$ and E_T separately from the detector corrected bins of $< Q_T >$ and E_T in the data, and then recalculating $< Q_T > / E_T$. Figure 19 shows the underlying event subtracted data where the solid lines represent the size of the total systematic uncertainty in the $< Q_T > / E_T$ versus E_T curve. Figure 19 and the size of the uncertainty are tabulated in Table 3.

5 Comparisons to Theoretical Predictions

5.1 Parton Level QCD Calculations

The calculations discussed in section 2 were based on QCD parton level calculations of $2 \Rightarrow 2$ and $2 \Rightarrow 3$ processes with no explicit treatment of hadronization. Before proceeding to a discussion of this topic it is useful to compare these calculations to the data. Figure 20 shows the data compared to the PAPAGENO parton level result. Although this QCD prediction does not explicitly include the effects of hadronization, it shows a level and shape of $< Q_T > /E_T$ which is similar to the data.

Also shown in the Figure is the result of a 3-body(parton) phase space calculation. Since $< Q_T > /E_T$ is a dimensionless quantity which is independent of the E_T in an event, the $< Q_T > /E_T$ curve is flat for the 3-body phase space parton level calculation.[30]

Note that all of the theoretical plots presented in this section were generated without an underlying event, since the data has already been corrected for that effect.

5.2 Fragmentation and Hadronization

The predictions for $< Q_T > /E_T$ discussed thus far were based on parton level calculations without any attempt to include the effects of converting these partons into hadrons. Since hadrons, not partons, are measured in the data, some study of the effect of this process is necessary. Hadronization is the soft, low energy ($Q^2 \approx \Lambda^2$) regime where quarks and antiquarks are clumped together into hadrons, whereas fragmentation includes both the contributions of gluon bremsstrahlung, as well as the hadronization of the partons. By evaluating the $2 \Rightarrow 3$ matrix element without imposing cuts

on the parton energies and separation, the parton calculation for $< Q_T > /E_T$ is, in a sense, including a first-order estimate of what is generally included in fragmentation. As shown by Ellis and Webber,[18] the additional Q_T from hadronization is expected to be small compared to the Q_T from gluon bremsstrahlung.

On the other hand, they do not consider events in which there is no gluon bremsstrahlung i.e. $2 \Rightarrow 2$ events, where hadronization would add Q_T to events which had zero Q_T at the parton level. To estimate the contribution of hadronization to $< Q_T > /E_T$, two approaches were used. The first employs full Monte Carlo simulation programs which perform parton-level calculations, gluon bremsstrahlung and hadronization. The second involves passing the output of a $2 \Rightarrow 2$ parton calculation (PAPAGENO version 3.09) through an independent hadronization program; both of these methods are discussed below.

Traditionally, the effects of fragmentation are incorporated into leading log Monte Carlo simulation programs. Two such programs are HERWIG[31] and ISAJET.[29] For this analysis, HERWIG version 3.2 and ISAJET version 5.38 were used. Both begin with a $2 \Rightarrow 2$ scattering and then use gluon bremsstrahlung to generate multiparton events. Each program cuts off the bremsstrahlung and uses a separate "hadronization" step to create the particles which will be detected.

In the case of ISAJET, after the bremsstrahlung has been completed, the Feynman-Field fragmentation functions are used to hadronize each parton independently. Here "fragmentation function" refers specifically to the hadronization of ISAJET partons. A cut-off on the gluon mass of 6 GeV limits the contribution of bremsstrahlung and defines the separation between the parton-level QCD processes and hadronization. Figure 21a shows separate $< Q_T > /E_T$ distributions for ISAJET partons and hadronization prod-

ucts. The parton calculation was performed on the "evolved partons", i.e. the quarks and gluons after bremsstrahlung has occurred. This illustrates the size of the effect of hadronization for this definition of the relative contributions of gluon bremsstrahlung and hadronization.

Unlike ISAJET, the HERWIG program takes into account the effects of gluon interference and coherence at the parton level. These considerations result in gluon branching angles that decrease as a shower progresses and in energy restrictions on the emitted gluons. Although HERWIG also must introduce an external cut-off on the emitted gluon mass, it is much lower (0.65 GeV) because the formalism is structured to take into account the low energy gluons. The HERWIG model is similar to the string fragmentation schemes and thus provides a very different estimate of the possible contribution to $< Q_T > /E_T$ from hadronization. Figure 21b shows separate $< Q_T > /E_T$ curves for the hadronization products and the partons from the HERWIG generator. As before, the parton level calculation of $< Q_T > /E_T$ uses the fully evolved (after bremsstrahlung stage has completed) quarks and gluons. The additional $< Q_T > /E_T$ which is attributed to hadronization is much smaller than in ISAJET as was expected from the lower cut-off on the gluon bremsstrahlung. Figure 22 shows the data compared with the HERWIG result for hadronized partons. HERWIG is in good agreement with the data over the complete E_T range.

In addition, another approach was developed in which the output of matrix element parton generators (i.e. PAPAGENO) can be hadronized. The program was based on the ISAJET routines which performed the Feynman-Field fragmentation, using a limited transverse momentum with respect to the parton axis. Since the parton level calculations (i.e. PAPAGENO) do not include additional gluon bremsstrahlung,

the parameters of the fragmentation function had to be adjusted. The PAPAGENO $2 \Rightarrow 2$ events were used as input and the fragmentation parameters were tuned to give agreement with di-jet data.

Naively one might attempt to apply this hadronization to the partons from the PAPAGENO $2 \Rightarrow 3$ calculation, but this is not possible. First, hadronization would add Q_T to events which previously had zero Q_T and thus the QCD divergence would no longer be cancelled. Second, by not imposing a cut-off on the radiated gluons, the original $< Q_T >$ calculation is, at some level, accounting for part of what is generally absorbed into the fragmentation functions and thus adding to this result would be "double counting".

To estimate the size of the contribution to $< Q_T > /E_T$ from this model of hadronization, PAPAGENO $2 \Rightarrow 2$ events were generated and hadronized and $< Q_T > /E_T$ was calculated from the hadronization products. In contrast to the tuning procedure, no di-jet cuts were applied to the generated events or the data. The resulting $< Q_T > /E_T$ curve is shown in Fig. 22 compared to the data. If no hadronization were performed, the $< Q_T > /E_T$ for the $2 \Rightarrow 2$ process would be identically zero. Clearly, this model of hadronization adds a significant amount of Q_T to the $2 \Rightarrow 2$ events, although it is not enough to bring the $2 \Rightarrow 2$ QCD prediction into agreement with the data. In other words, the effect of hard gluon bremsstrahlung must be included to achieve the level of $< Q_T > /E_T$ observed in the data.

It is instructive to determine the main contribution to the $< Q_T >$ in the event, i.e. is it from particles near the thrust axis or at wide angles? To examine this, the fractional Q_T contribution of each tower in an event has been plotted as a function of the angle ϕ between the tower and the thrust axis. Figure 23 shows this distribution

summed over events in different E_T bins. The corrections for detector effects that could change the shape of this distribution, such as the track correction for the nonlinearity, have been applied. Since the Monte Carlo based detector corrections were simply overall factors, they would not change the shape of this distribution and thus they have not been included. A correction for the underlying event has been applied by following the assumption of an isotropic underlying event energy distribution and using the underlying energy density measurement discussed in Section 4 and Ref. 30.

Figure 23 also shows the same distributions for HERWIG hadronized partons (solid curve) and from the hadronized PAPAGENO $2 \Rightarrow 2$ events (dotted curve). Statistical fluctuations in the Monte Carlo distributions have been smoothed for clarity. Each of these distributions has been normalized to the same area as the corresponding distribution for real data. Except in the lowest E_T interval, near the experimental trigger threshold, the HERWIG plots show remarkably similar shape to the data over the E_T range covered in the plots. The $2 \Rightarrow 2$ curves show too much peaking near the thrust axis and too little contribution at wide angles. This is as expected since the region near the thrust axis is what was specifically included in the $2 \Rightarrow 2$ plus hadronization model while no attempt was made to reproduce the wide angle behavior. Comparing these PAPAGENO $2 \Rightarrow 2$ and HERWIG curves with the data and with the $< Q_T > / E_T$ vs. E_T results from each model indicates that while there is a significant contribution to $< Q_T >$ near the thrust axis, the wide angle contributions are also important in determining the mean.

6 Conclusions

We have measured the average value of the global event parameter, Q_T , as a function of E_T in $\bar{p}p$collisions at 1.8 TeV. Measurement of Q_T in the CDF data is an important test of QCD predictions in the region generally excluded from clustering types of analysis. A QCD parton level calculation is consistent with the experimental measurements, as is a full leading-log Monte Carlo program, HERWIG, which includes the effect of a running coupling constant, coherent multiple gluon emission and hadronization. In addition, the HERWIG Monte Carlo describes well the observed shape of the angular distribution of individual calorimeter tower contributions to Q_T within the events.

Since Q_T is sensitive to energy depositions away from the jets, the underlying event, unavoidably present in experimental data, introduces a large correction and uncertainty. The effect of the underlying event was estimated from the data by measuring the energy density at wide angles from the jets, but the contribution of the hard scattering in that region is not well defined.

In order to judge the sensitivity of comparisons between data and theoretical predictions, two other models were studied: a three-parton phase space model, and a $2 \Rightarrow 2$ parton level calculation with hadronization. Neither was consistent with the experimental measurements. From these results, it appears that hard gluon emission, as predicted by QCD, is necessary to describe the data.

Independent of the experimental data, the Monte Carlo studies have taught us much about the behavior of Q_T . Although it has been argued[18] that Q_T is insensitive to soft hadronization effects, careful Monte Carlo studies reveal a sensitivity to the definition of the division between hadronization and gluon bremsstrahlung. The effect of hadronization is fundamentally a theoretical issue and cannot be separated experimen-

tally from the effects of gluon bremsstrahlung. Thus, we have not attempted to unfold the effects of hadronization from the data, and comparisons are made either to parton level predictions directly, or to hadronized parton calculations where appropriate.

The parton level calculation suggested that the average value of Q_T as a function of E_T is sensitive to the running of the strong coupling constant. Monte Carlo studies show that this sensitivity is substantially reduced when contributions to Q_T are summed only over the central rapidity region. This significance is also reduced by a large uncertainty from the ambiguities associated with hadronization. Thus, our studies demonstrate that this suggestion, based on parton distributions, is overly optimistic because the running of the strong coupling constant cannot be isolated from other effects in observable hadron distributions.

7 Acknowledgements

We thank the Fermilab Accelerator Division, the Computer Division and the technical staffs of CDF and the collaborating institutions for their effort in the construction and operation of the Tevatron, the Antiproton Source and this experiment. This work was supported by the Department of Energy, the National Science Foundation, Istituto Nazionale di Fisica Nucleare, the Ministry of Science, Culture and Education of Japan, and the A. P. Sloan Foundation.

References

[1] G. Hanson et al., Phys. Rev. Lett. 35, 1609 (1975).

[2] Ch. Berger et al.(PLUTO Collaboration), Phys. Lett. 78B, 176 (1978).

[3] D.P. Barber et al.(MARK-J Collaboration), Phys. Rev. Lett. 43, 830 (1979).

[4] R. Brandelik et al.(TASSO Collaboration), Phys. Lett. 86B, 243 (1979).

[5] Ch. Berger et al.(PLUTO Collaboration), Phys. Lett. 86B, 418 (1979).

[6] D.P. Barber et al.(MARK-J Collaboration), Phys. Lett. 89B, 139 (1979).

[7] W. Bartel et al.(JADE Collaboration), Phys. Lett. 91B, 142 (1980).

[8] R. Brandelik et al.(TASSO Collaboration), Phys. Lett. 94B, 437 (1980).

[9] S.D. Ellis, Phys. Lett. 97B, 459 (1980).

[10] J. Dorfan, Proceedings of the International Lepton/Photon Symposium-Cornell University p. 686 (1983).

[11] W. De Boer, SLAC-PUB-4428, September, 1987, (unpublished).

[12] T. Akesson et al.(AFS Collaboration), Z. Phys. C30, 27 (1986).

[13] R. Ansari et al.(UA2 Collaboration), Z. Phys. C36, 175 (1987).

[14] Ch. Berger et al.(PLUTO Collaboration), Phys. Lett. 97B, 459 (1980).

[15] M. Banner et al.(UA2 Collaboration), Phys. Lett. 118B, 203 (1982).

[16] F. Abe et al.(CDF Collaboration), Phys. Rev. Lett. 62, 613 (1989).

[17] F. Abe et al.(CDF Collaboration), Phys. Rev. Lett. 62, 3020 (1989).

[18] R.K. Ellis and B.R. Webber, "Procceedings of the 1986 Summer Study on the Physics of the Superconducting Supercollider" edited by R. Donaldson and J. Marx, p. 74, Snowmass Co. (1986).

[19] F. Halzen and A.D. Martin, Quarks and Leptons: An Introductory Course in Modern Particle Physics, John Wiley and Sons Inc., (1984).

[20] D.W. Duke and J.F. Owens Phys. Rev. D 30, 49 (1984).

[21] Ian Hincliffe, Monte Carlo Program PAPAGENO, in preparation, (1990).

[22] Michelangelo Mangano, private communication.

[23] F. Abe et al.(CDF Collaboration), Nucl. Inst. and Meth. A271, 387 (1988).

[24] F. Snider et al., Nucl. Inst. and Meth. A268, 75 (1988).

[25] F. Bedeschi et al., Nucl. Inst. and Meth. A268, 50 (1988).

[26] L. Balka et al., Nucl. Inst. and Meth. A267, 272 (1988).

[27] S. Bertolucci et al., Nucl. Inst. and Meth. A267, 301 (1988).

[28] D. Amidei et al., Nucl. Inst. and Meth. A269, 51 (1988).

[29] Monte Carlo Event Generator for pp and $p\bar{p}$ Reactions: Version 5.38, written by Frank E. Paige and Serban D. Protopopescu, Brookhaven National Laboratory, BNL 38034 (1986).

[30] B.L. Flaugher, Ph.D. Thesis, Rutgers University, October, 1989 (unpublished).

[31] G. Marchesini and B.R. Webber, Cavendish-HEP-87/8, UPRF-87-212, Dec. (1987).

Table 1: Trigger Thresholds and Luminosity

E_t	Integrated Luminosity	Trigger Name
20 GeV	0.406 nb^{-1}	$SUM-ET-20$
30 GeV	11.620 nb^{-1}	$SUM-ET-30$
40 GeV	5.800 nb^{-1}	$SUM-ET-40$
45 GeV	5.771 nb^{-1}	$SUM-ET-45$

Table 2: E_T Cuts on Track Corrected Data

E_t	Number of Events	Trigger Name
70 GeV	7093	$SUM-ET-20$
85 GeV	33168	$SUM-ET-30$
100 GeV	3222	$SUM-ET-40$
120 GeV	1707	$SUM-ET-45$

Table 3: Table of $< Q_T > /E_T$ and E_T with statistical and systematic uncertainties, as shown in Fig. 19. A small asymmetry in the systematic uncertainty has been ignored here; only the average magnitude of the positive and negative contributions is given.

E_t (GeV)	$< Q_T > /E_T$	Stat.	Avg. Sys.
71	0.399	0.007	0.145
81	0.353	0.006	0.135
90	0.344	0.002	0.130
101	0.324	0.003	0.125
110	0.308	0.003	0.120
121	0.294	0.004	0.110
131	0.290	0.004	0.105
141	0.275	0.006	0.095
151	0.263	0.007	0.090
161	0.254	0.008	0.085
171	0.254	0.009	0.080
181	0.258	0.013	0.079
191	0.234	0.015	0.075
201	0.283	0.017	0.070
212	0.237	0.019	0.066
222	0.266	0.027	0.065
233	0.231	0.028	0.063
251	0.232	0.028	0.058
272	0.239	0.025	0.053
296	0.211	0.026	0.051
384	0.222	0.039	0.043

List of Figures

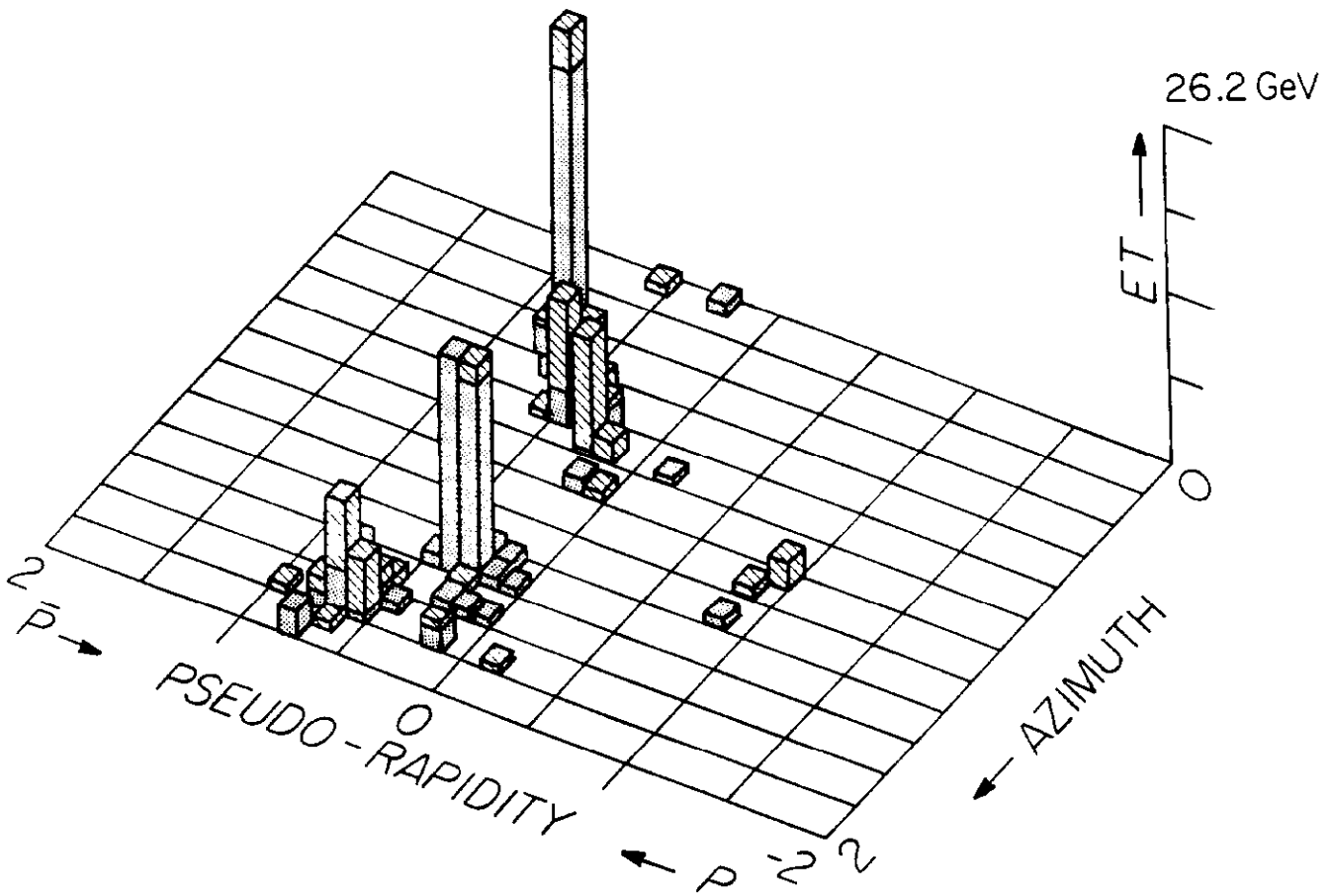

Figure 1: A CDF Jet event. The cylindrical calorimeter has been 'unrolled' such that the axes of the grid represent the azimuthal angle around the beamline, and the pseudo-rapidity, defined as $-ln(tan(\theta/2))$, where θ is the polar angle with respect to the beamline. The height of each cell is proportional to its transverse energy, $E_T = Esin\theta$.

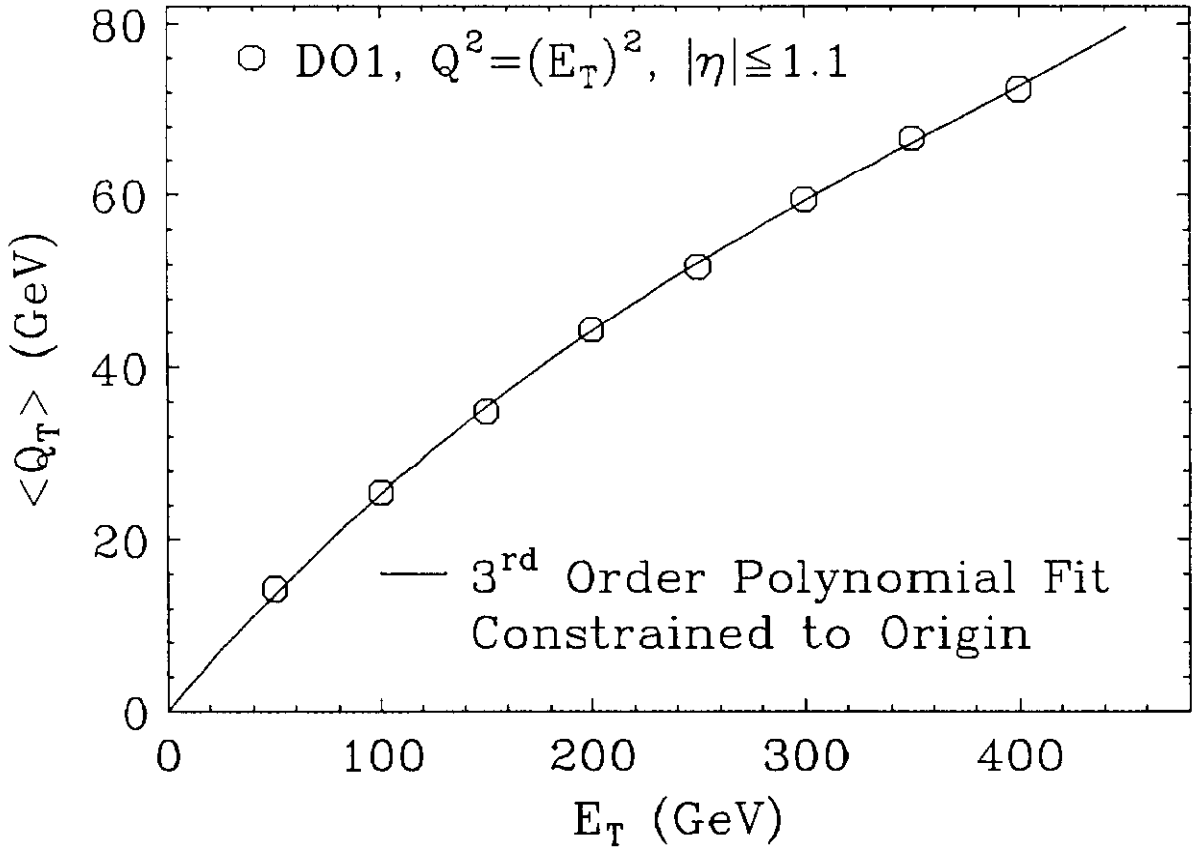

Figure 2: $< Q_T >$ using Duke and Owens structure functions set 1, $Q^2 = E_T^2$, and integrated over the range $|\eta| \leq 1.1$.

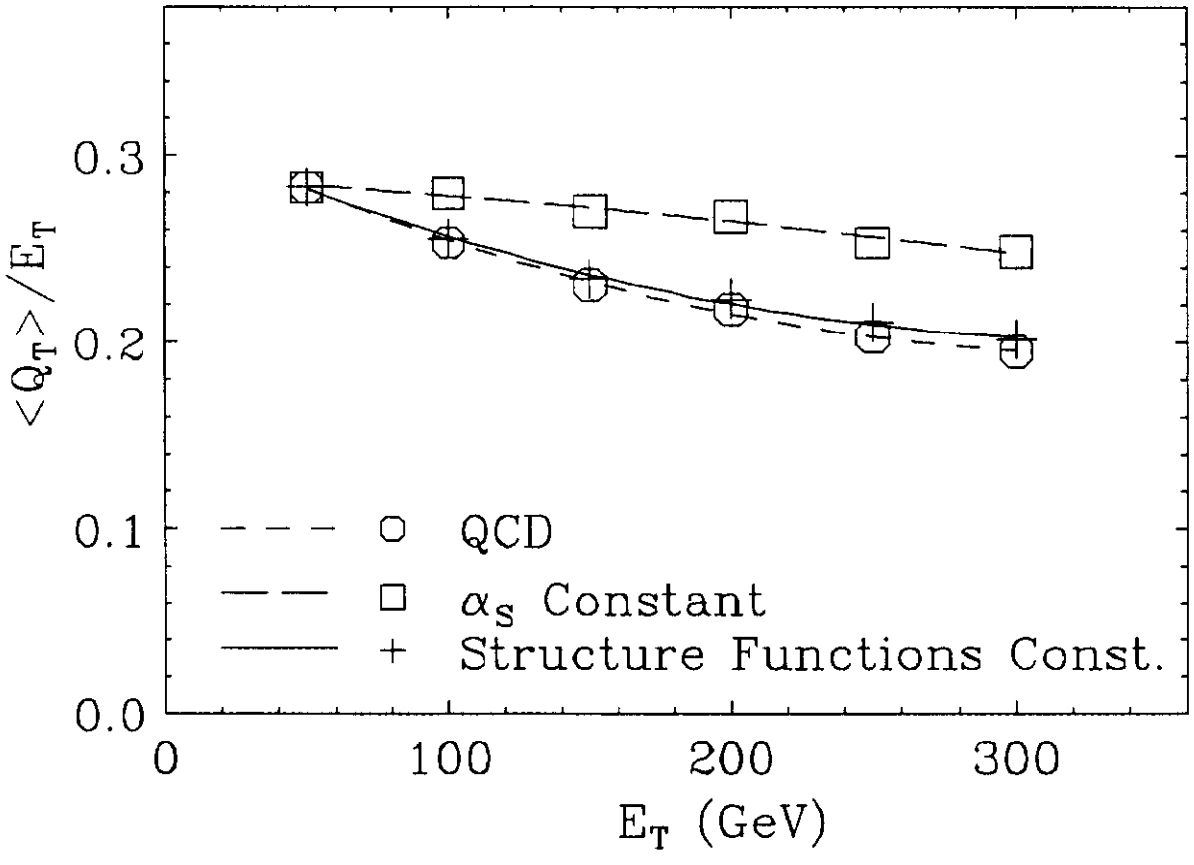

Figure 3: $< Q_T > /E_T$ for three scenerios: QCD; α_s running with no structure function evolution; α_s constant with standard structure function evolution. All use Duke and Owens set 1, $Q^2 = E_T^2$, over the range $|\eta| \leq 1.1$.

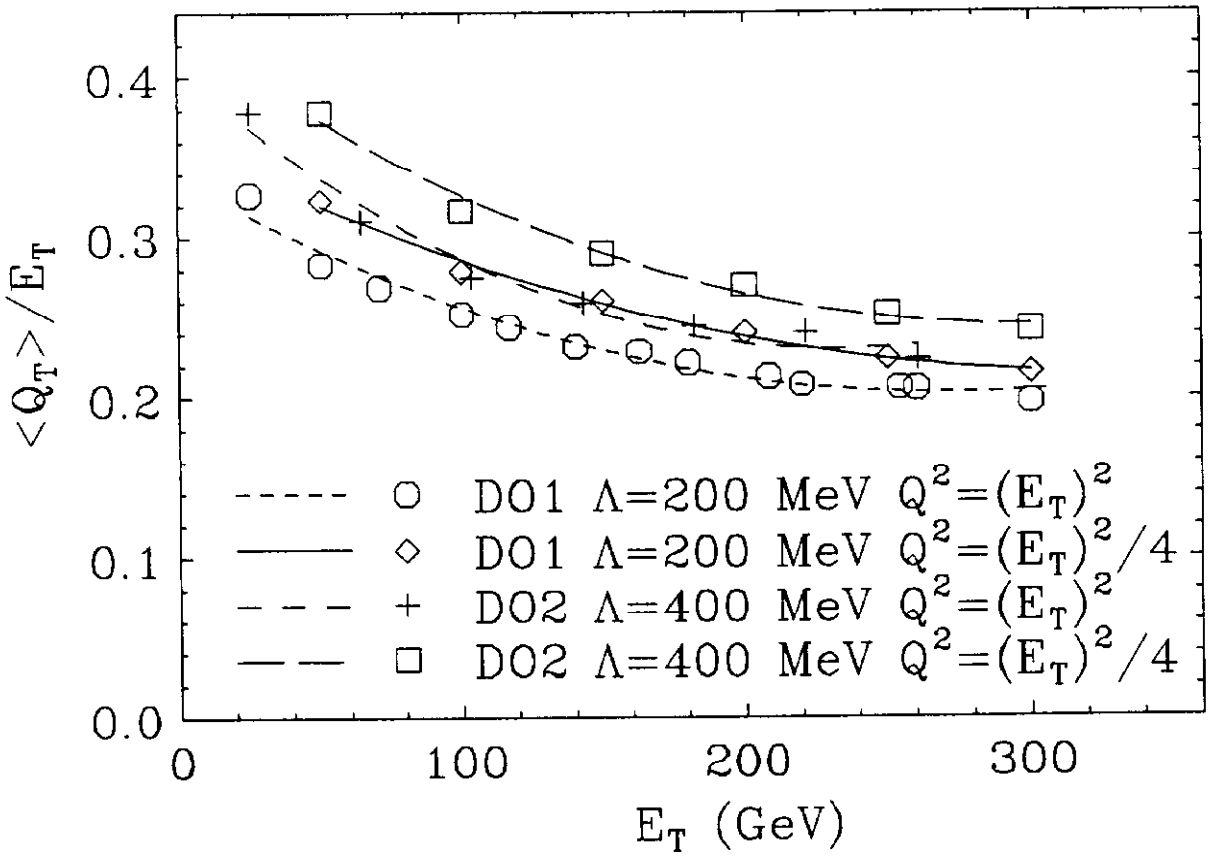

Figure 4: $< Q_T > / E_T$ for Duke and Owens sets 1 and 2 with scales of $Q^2 = E_T^2$ and $E_T^2/4$, for the range $|\eta| \leq 1.1$.

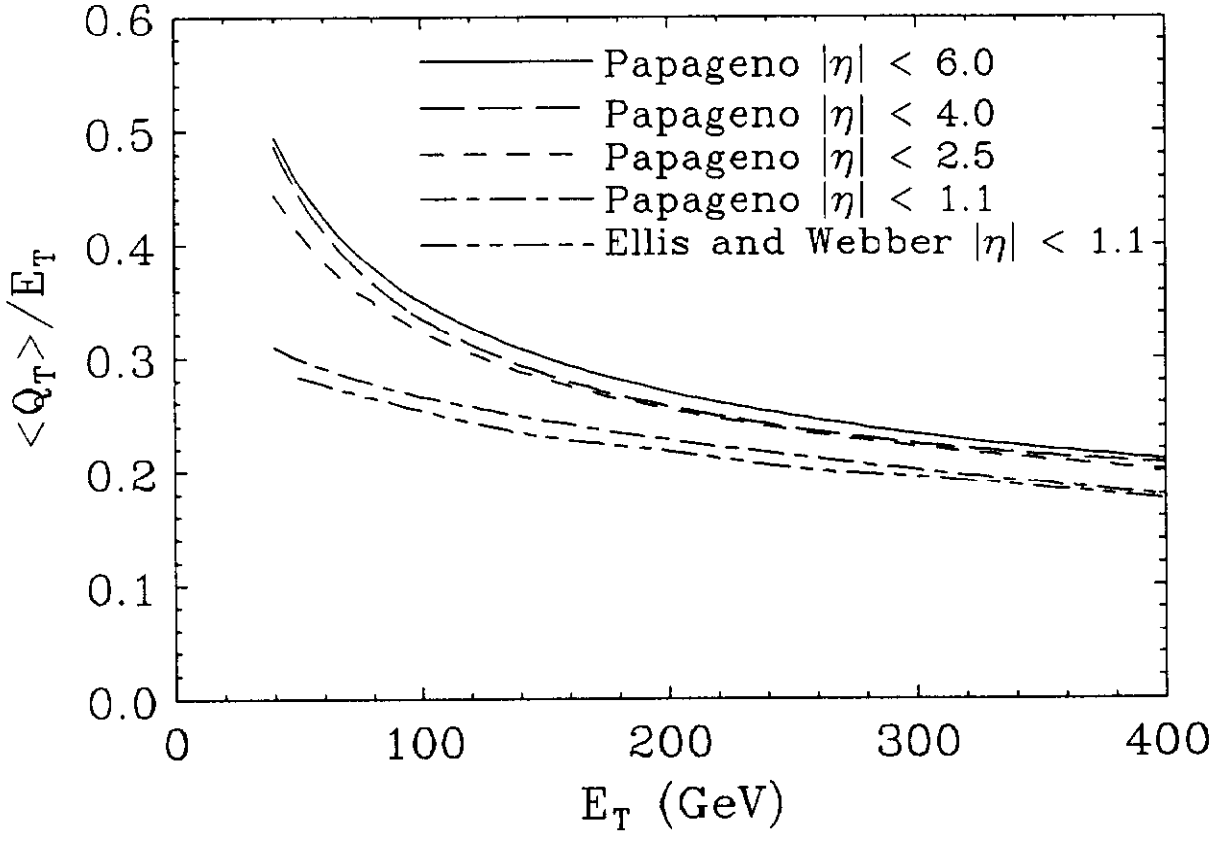

Figure 5: $< Q_T > / E_T$ vs. E_T calculated from partons which fall within the central ($|\eta| \leq 1.1$) region, for a variety of rapidity ranges used in the PAPAGENO event generation. Also, a comparison to the Ellis and Webber calculation is shown.

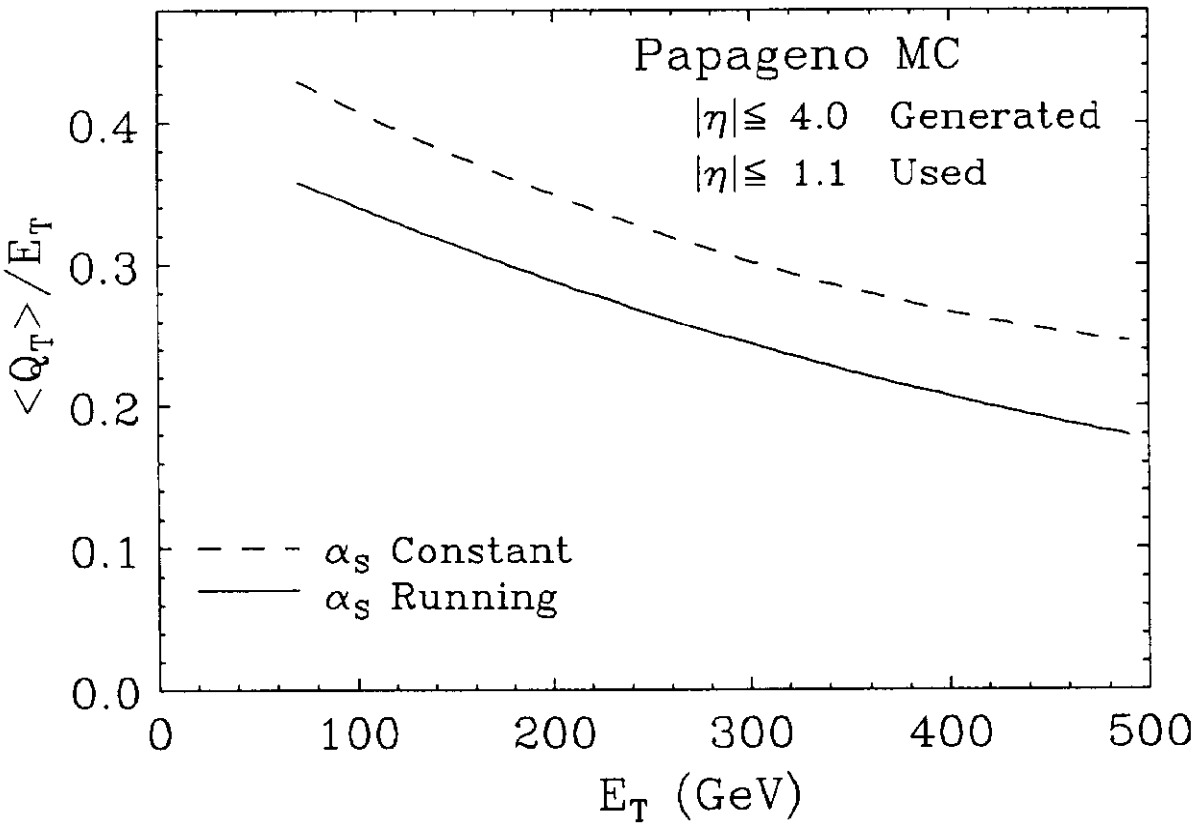

Figure 6: $< Q_T > / E_T$ vs. E_T for α_s constant and α_s running. Both curves were calculated from partons which fall within the central ($|\eta| \leq 1.1$) region, and a rapidity range of ($|\eta| \leq 4.0$) was used in the PAPAGENO event generation.

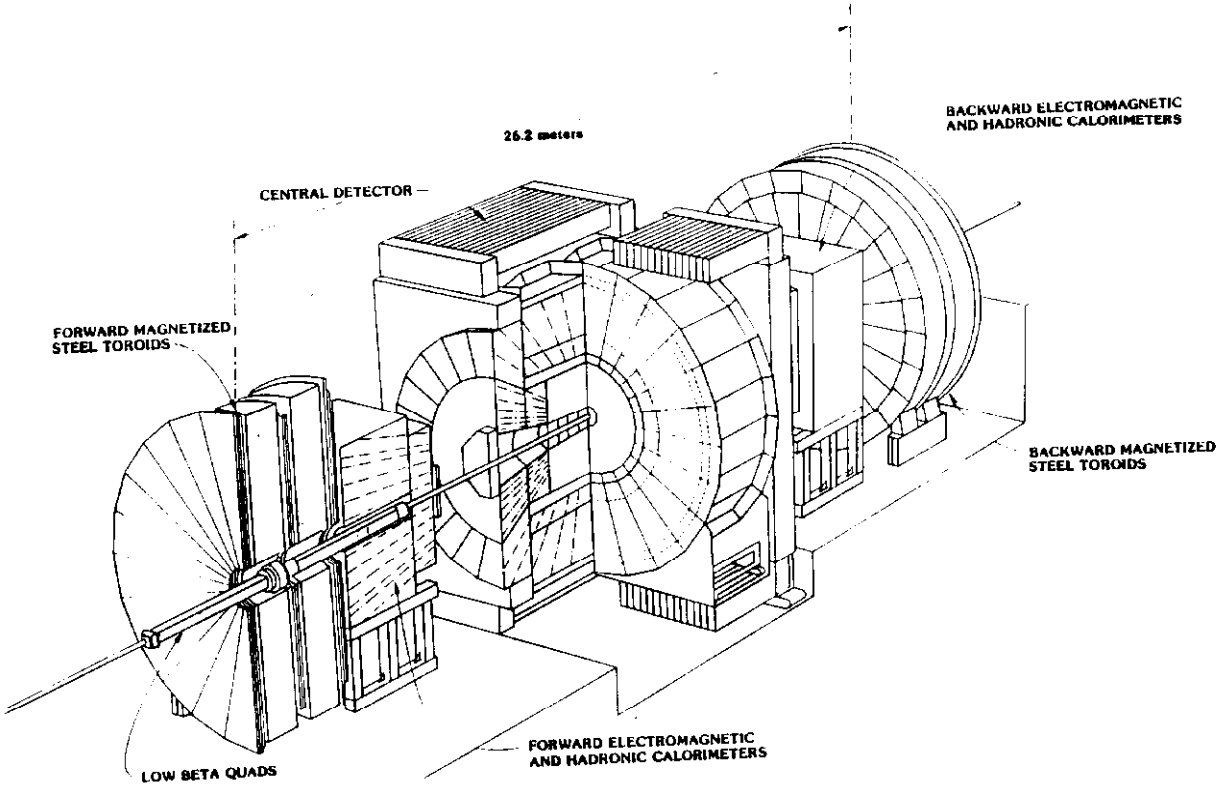

Figure 7: Perspective view of the components of the Collider Detector at Fermilab

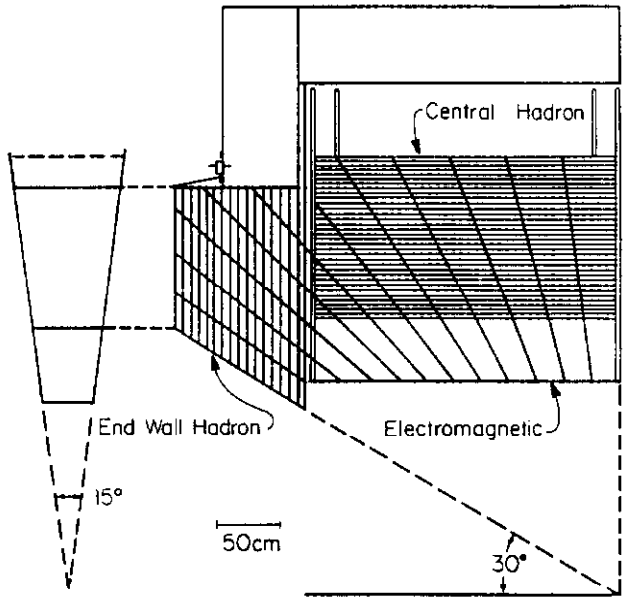

Figure 8: Projective tower structure of the CDF Central Calorimeters. The End Wall calorimeters are treated as part of the central region.

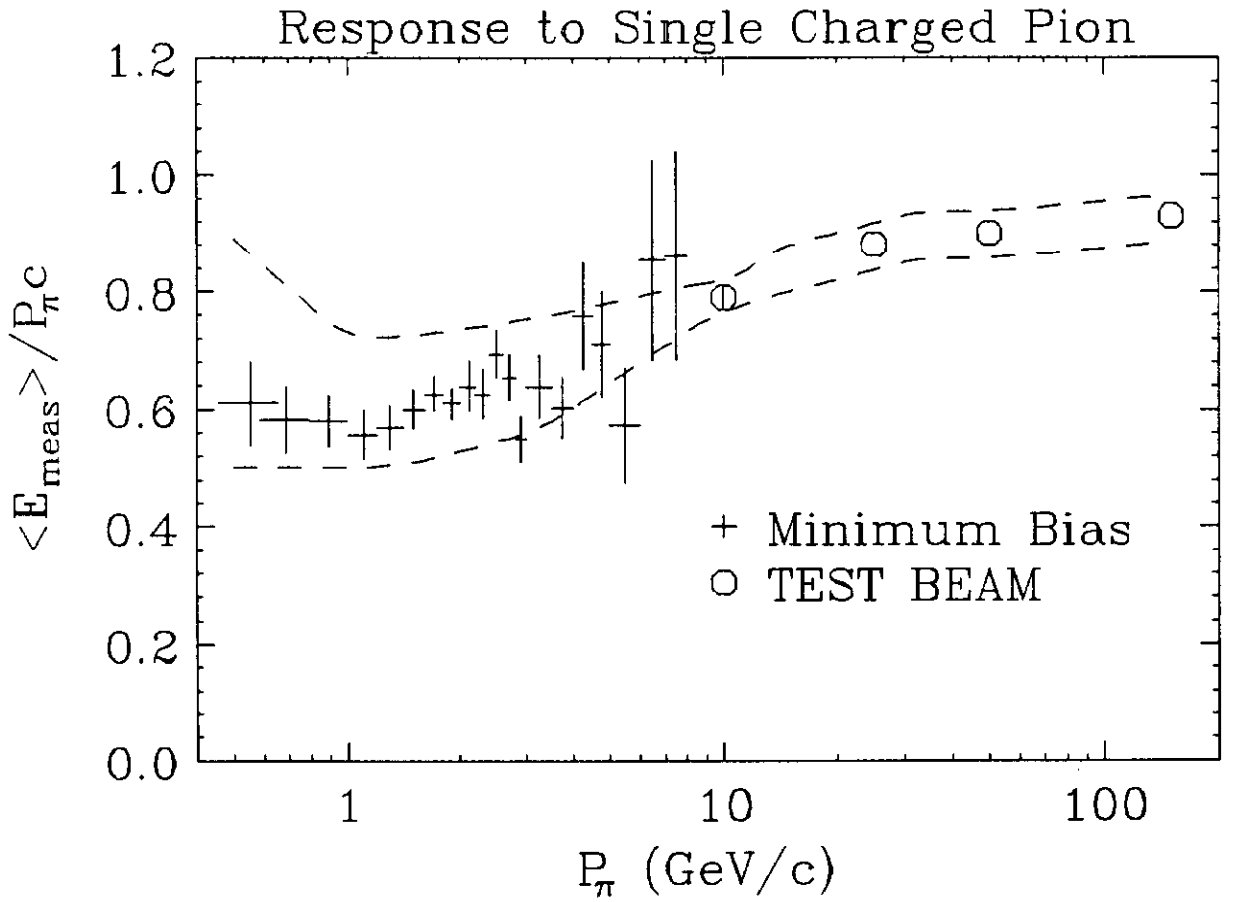

Figure 9: Average response of the central calorimeter to charged particles. Below 10 GeV minimum-bias isolated track data was used. Points above 10 GeV were derived from test beam studies. The curves represent the estimated size of the uncertainty in the determination of the average response.

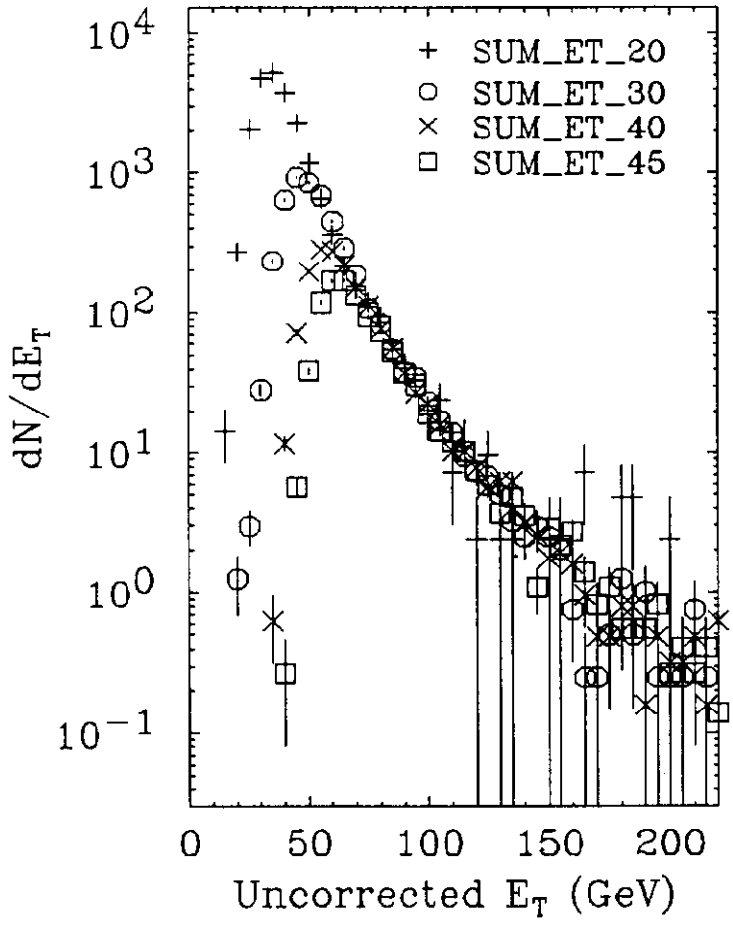

Figure 10: Uncorrected E_T spectrum for the separate trigger samples. The samples have been normalized by their relative luminosities.

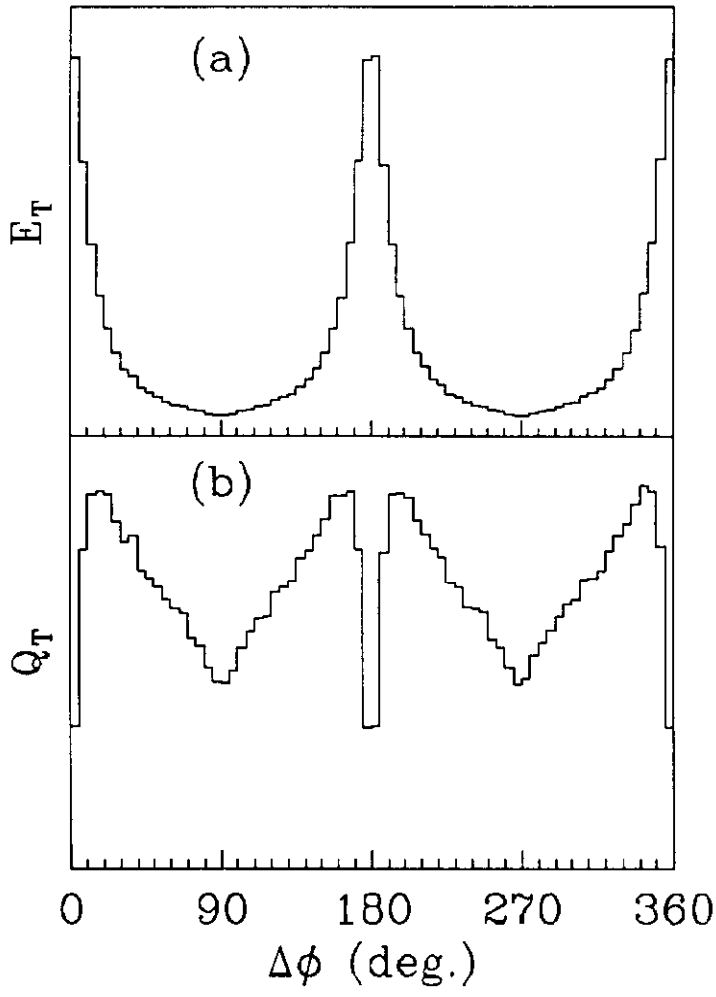

Figure 11: Relative E_T and Q_T distributions with respect to the transverse thrust axis. Each tower is entered such that the horizontal axis represents the angle $\Delta\phi$ between the tower and the thrust axis. The height corresponds to the E_T (Q_T) of the tower. This plot represents the sum over the data with a 30-GeV trigger threshold.

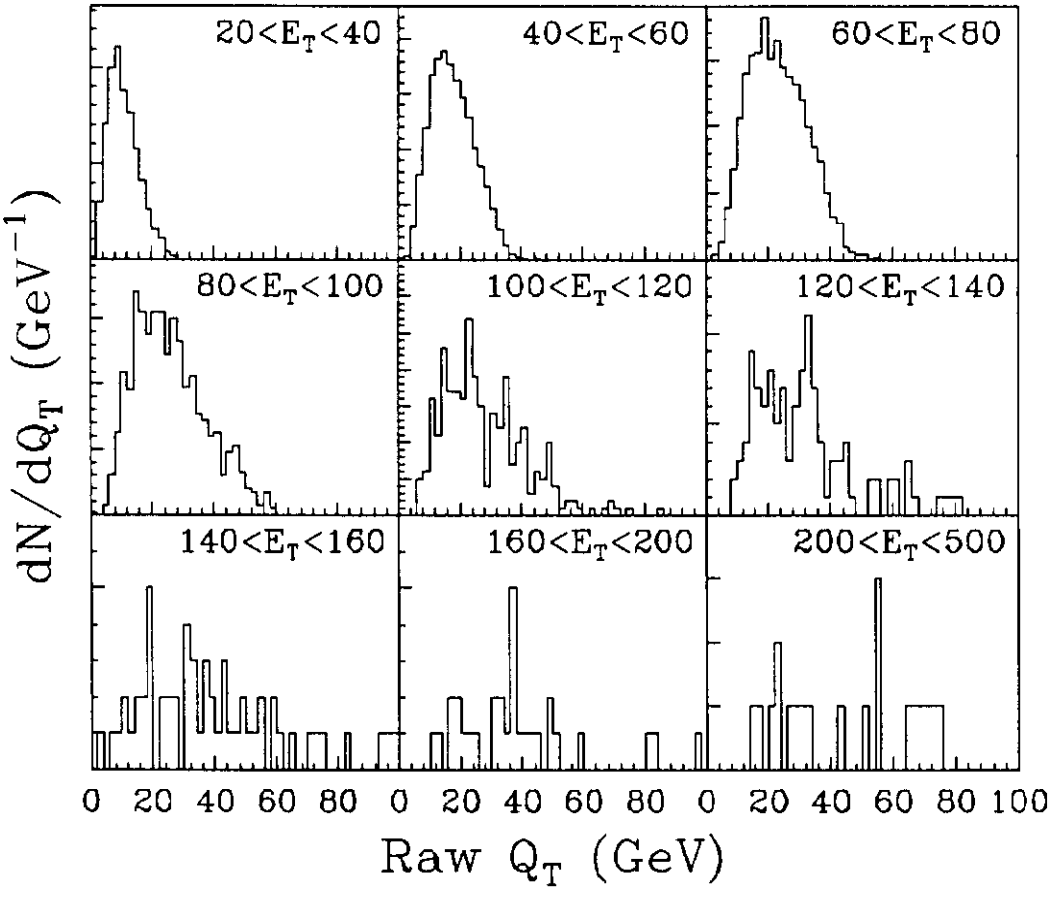

Figure 12: Q_T distributions in various E_T intervals. Vertical scales are normalized to the peak bin in order to emphasize the change in shape with E_T .

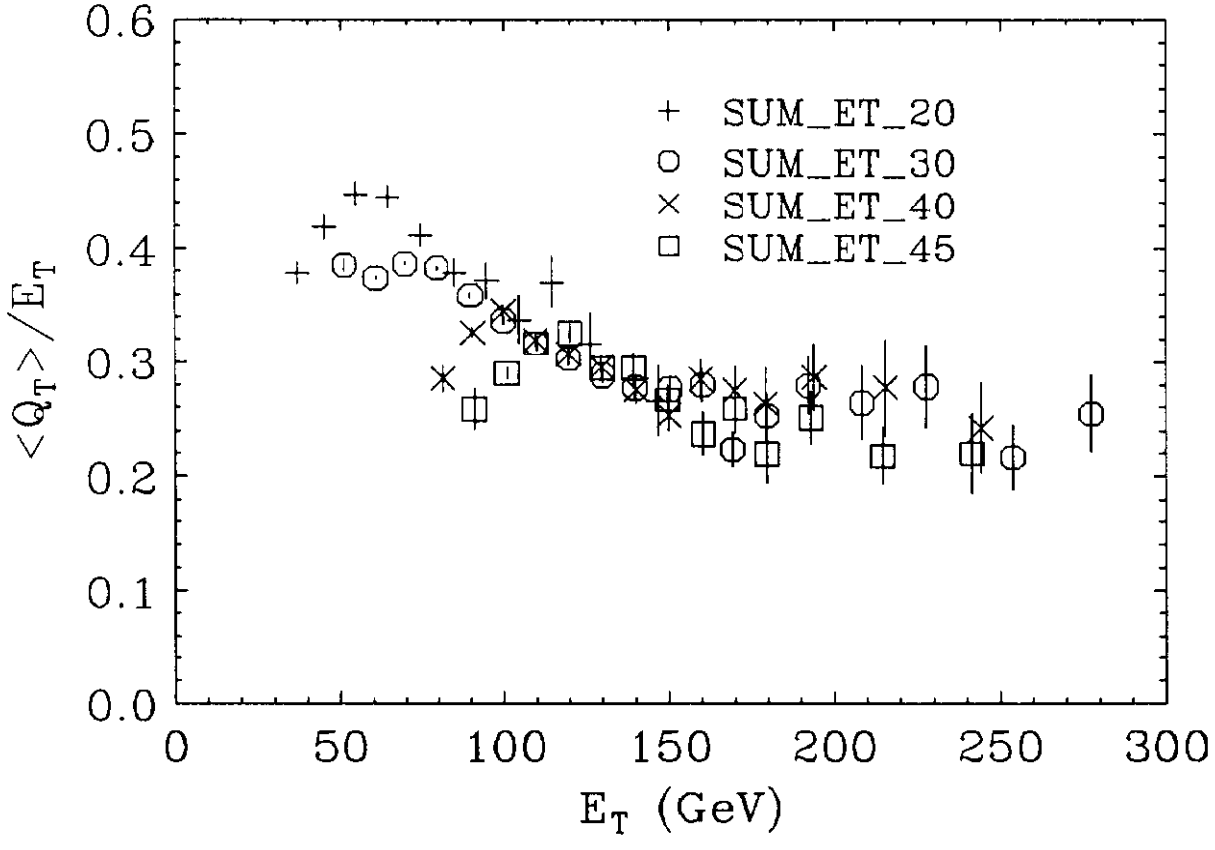

Figure 13: Track-corrected $< Q_T > /E_T$ for the separate trigger samples. No relative normalization is necessary since $< Q_T > /E_T$ is independent of the number of events in the sample. The overlap of the samples was used to determine the regions where the trigger was efficient.

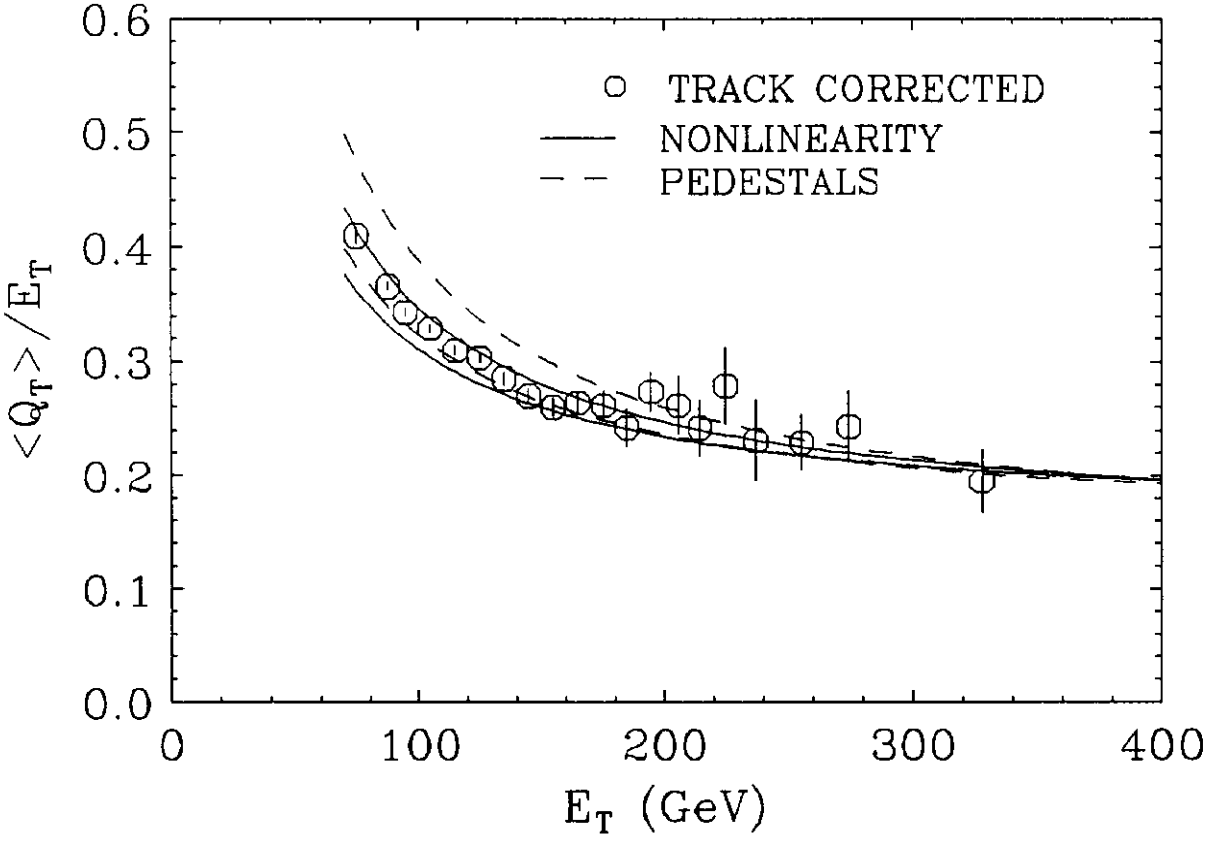

Figure 14: $< Q_T > /E_T$ curve for the track-corrected merged trigger samples, solid lines indicate the range of uncertainty in $< Q_T > /E_T$ from the uncertainty in the nonlinear response, dashes indicate size of uncertainty from pedestals.

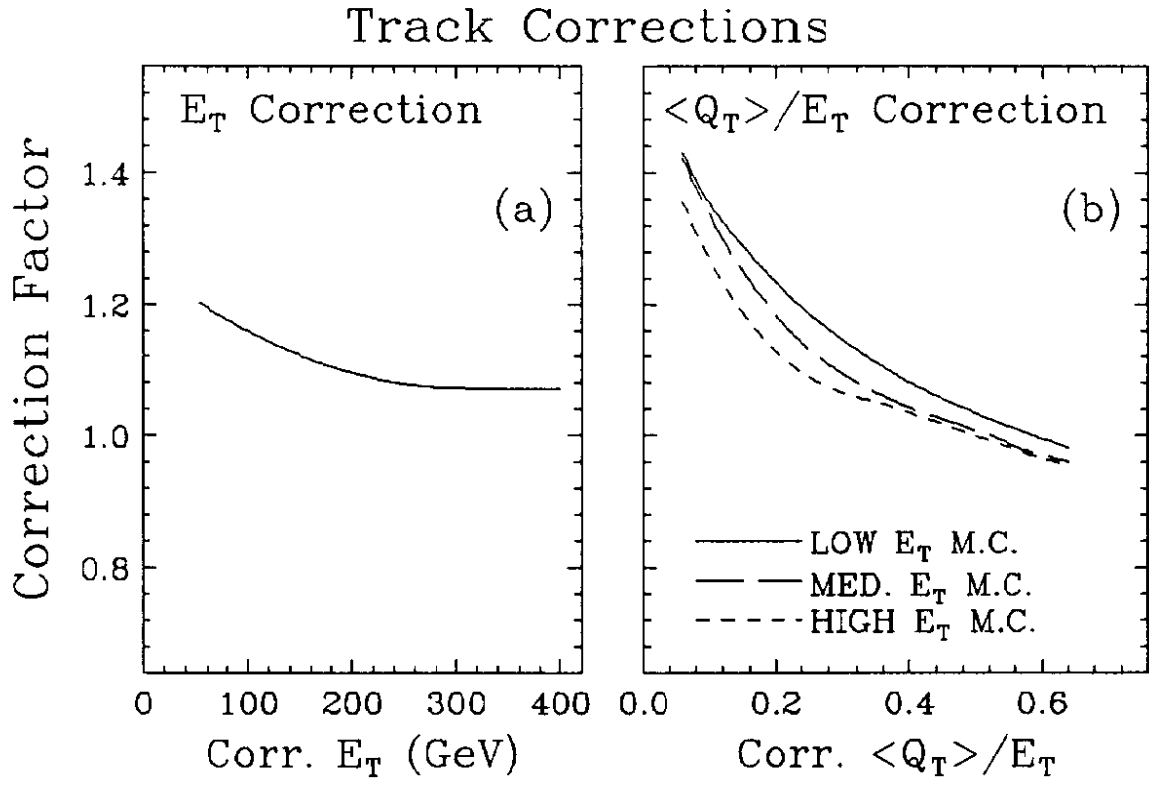

Figure 15: a) mean E_T correction factor as a function of track corrected E_T and b) Q_T/E_T correction factors for slices of track corrected E_T where LOW corresponds to 50-80 GeV, MED. corresponds to 100-140 GeV, and HIGH corresponds to 180-220 GeV.

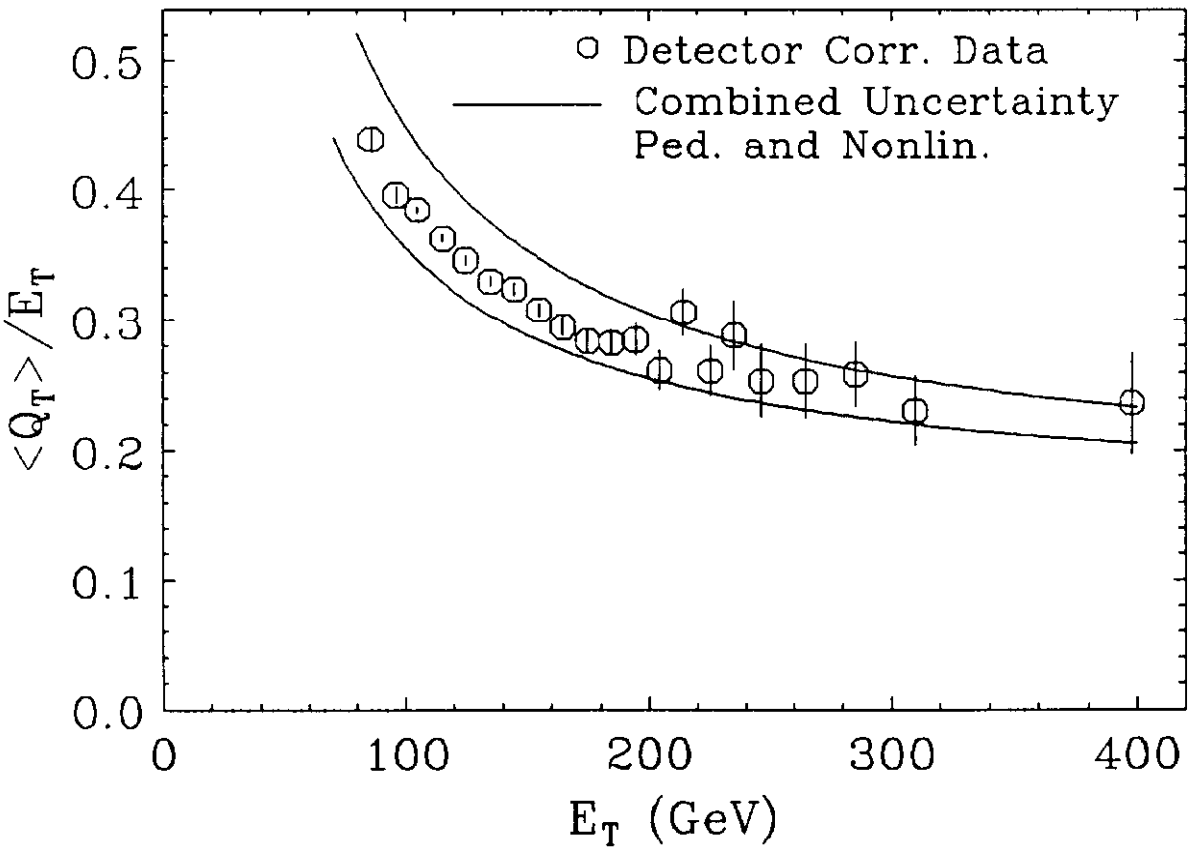

Figure 16: Detector corrected $< Q_T > /E_T$ vs E_T . The solid lines indicate the total systematic uncertainty. No correction for the underlying event has been performed.

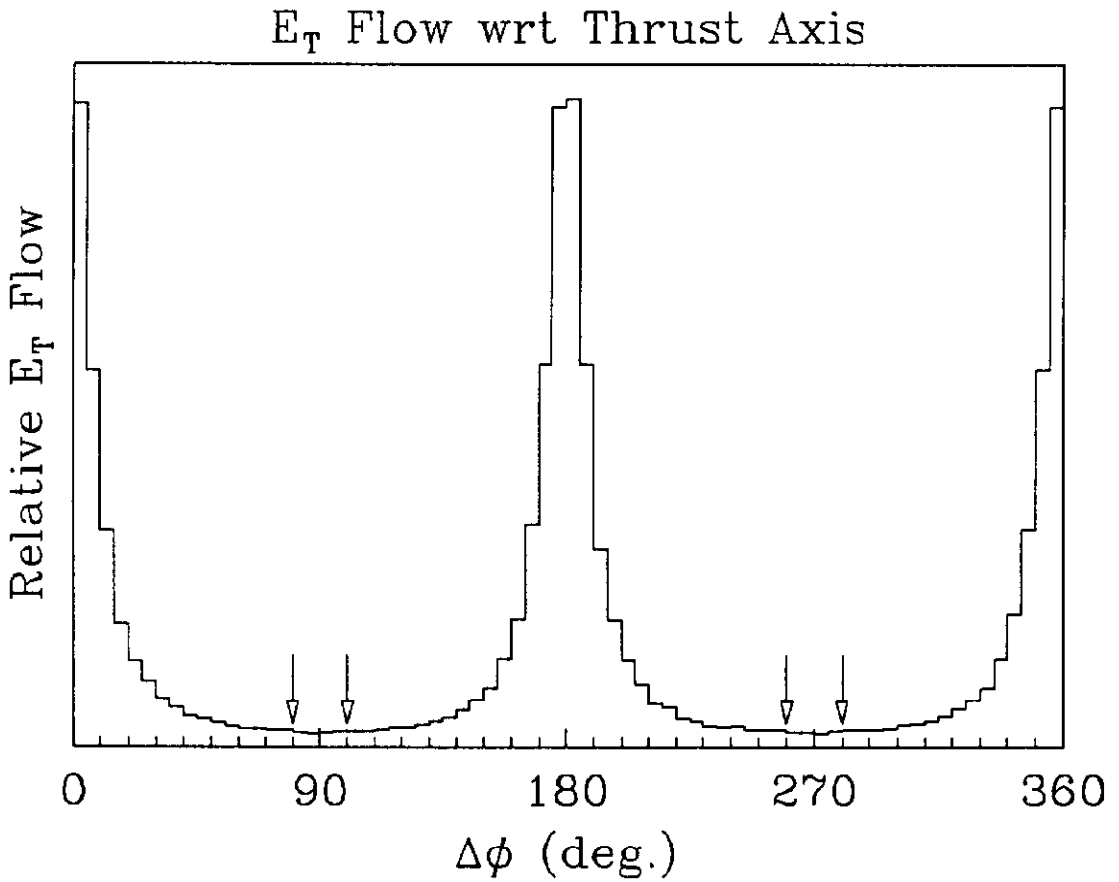

Figure 17: The E_T flow with respect to the thrust axis for di-jet events. Each tower is entered such that the horizontal axis represents the angle $\Delta\phi$ between the tower and the thrust axis. The height represents the E_T of the tower. The arrows indicate the angular region that was used for the underlying event measurement.

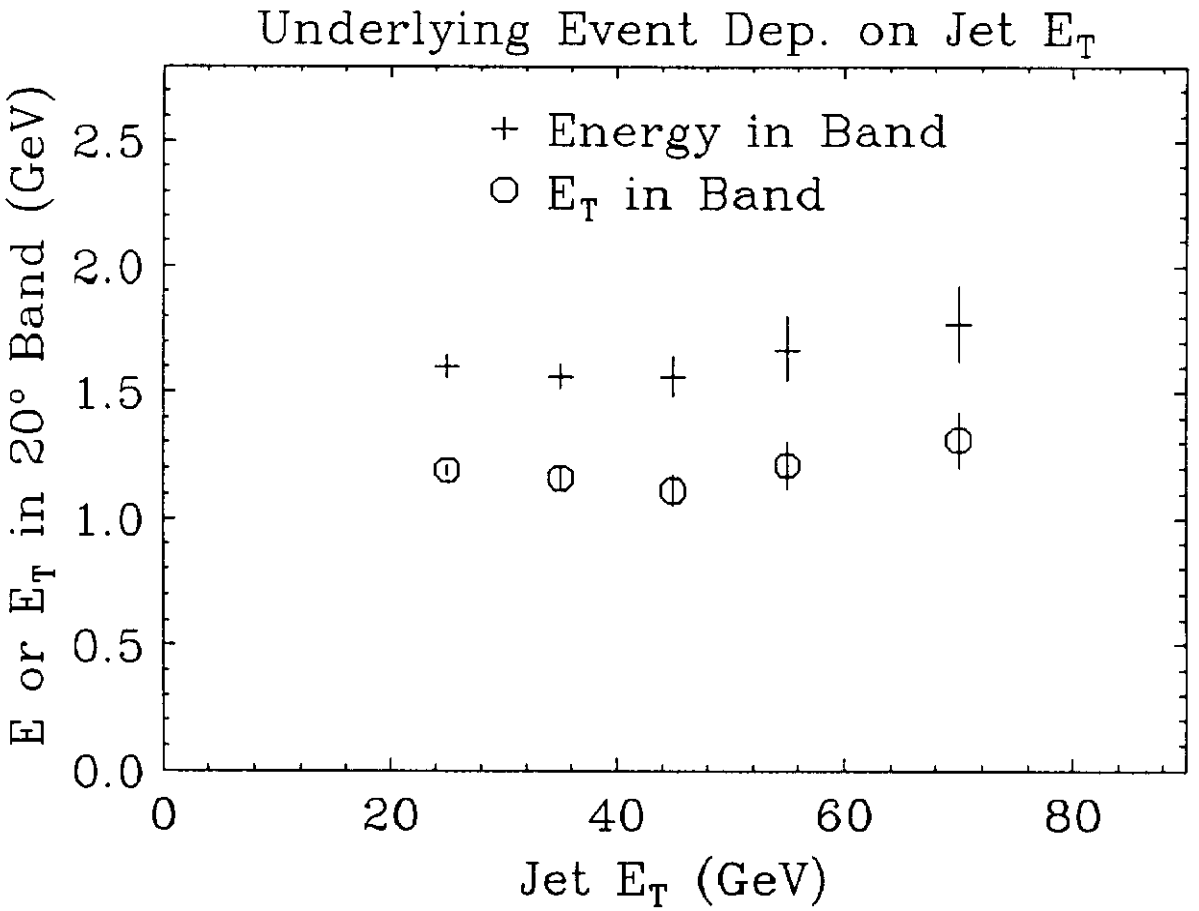

Figure 18: Underlying event E_T vs. average cluster E_T. Di-jet cuts required two clusters of $E_T \geq 20$ GeV and that these clusters be back-to-back within 10° in ϕ.

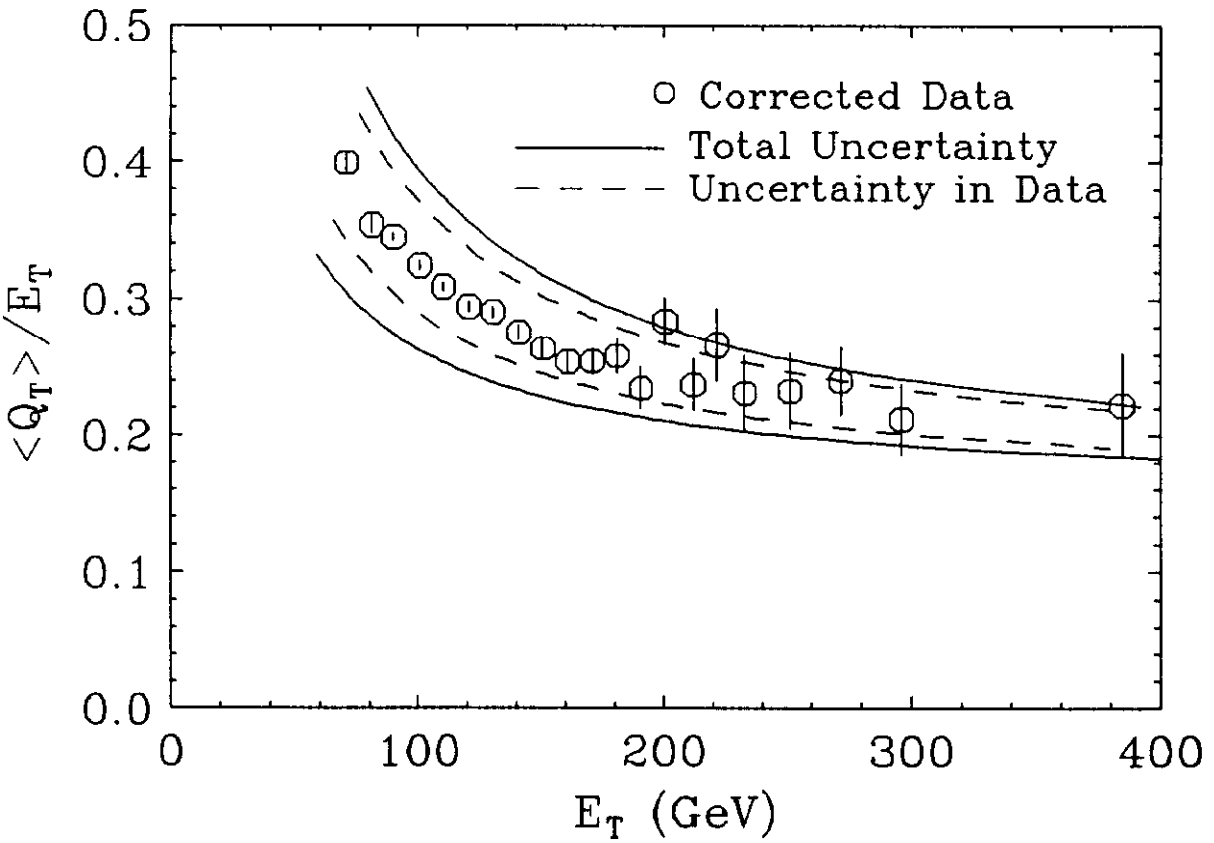

Figure 19: Final $< Q_T > /E_T$ vs. E_T curve. The underlying event has been subtracted. The dashed lines indicate the uncertainty in the measurement of $< Q_T > /E_T$. The solid lines represent total systematic uncertainty.

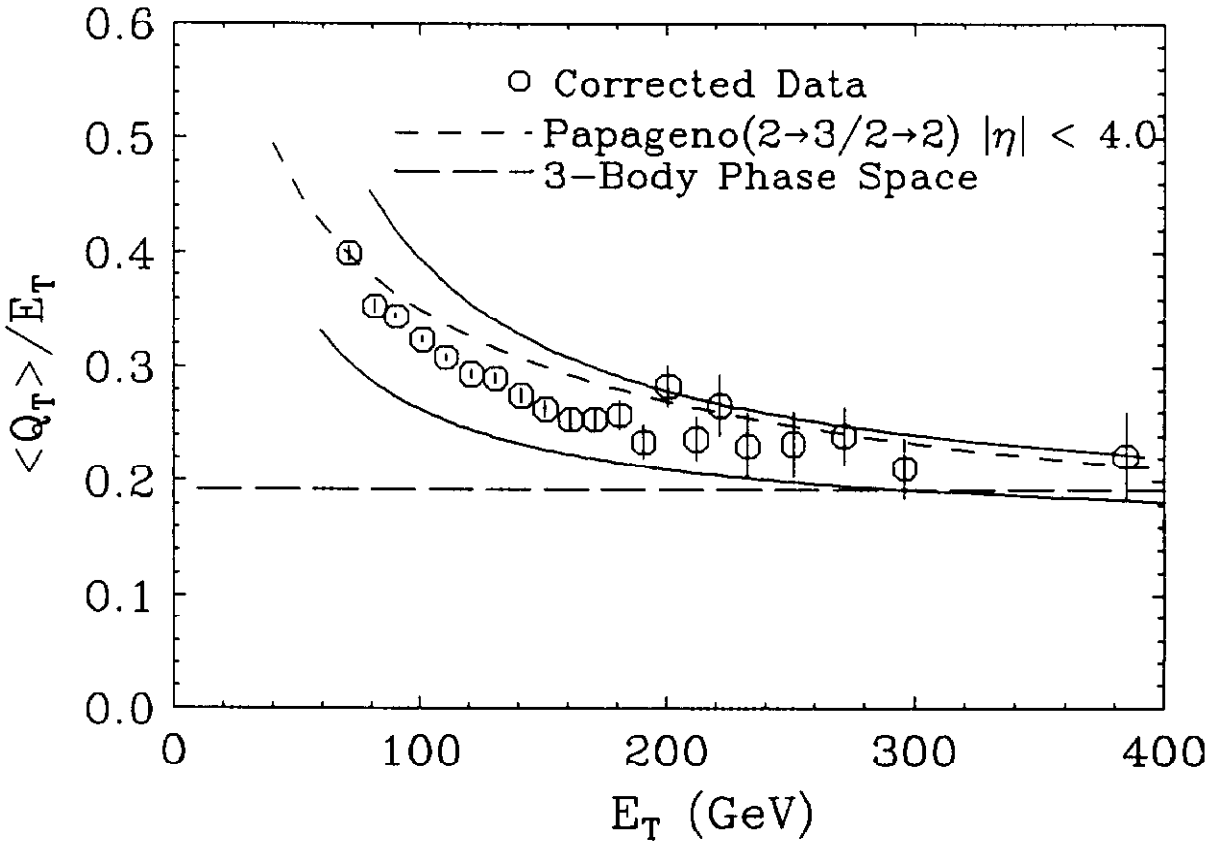

Figure 20: $< Q_t > /E_t$ vs. E_t for data compared to PAPAGENO $< Q_T > /E_T$ parton level prediction and parton level 3 body phase space.

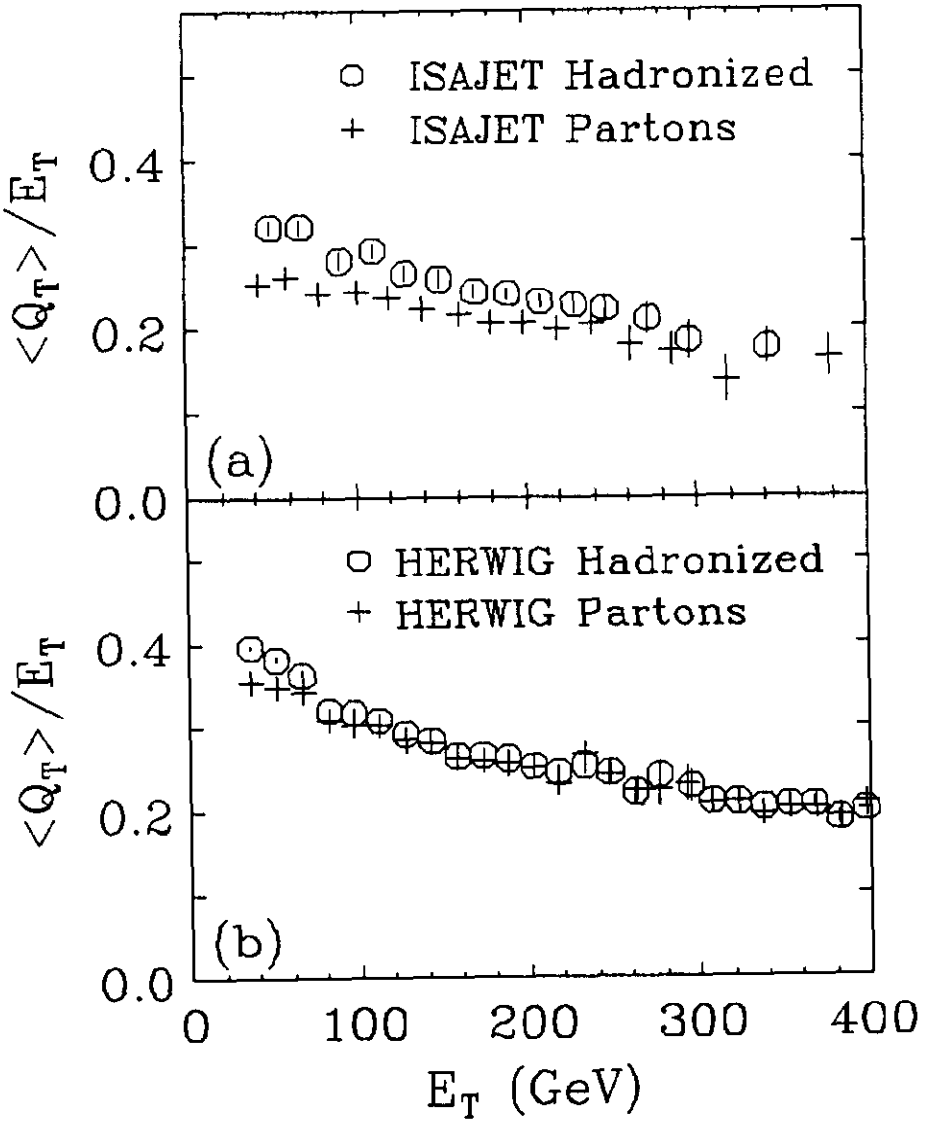

Figure 21: $< Q_T > /E_T$ vs. E_T for a) ISAJET and b) HERWIG partons and hadronization products.

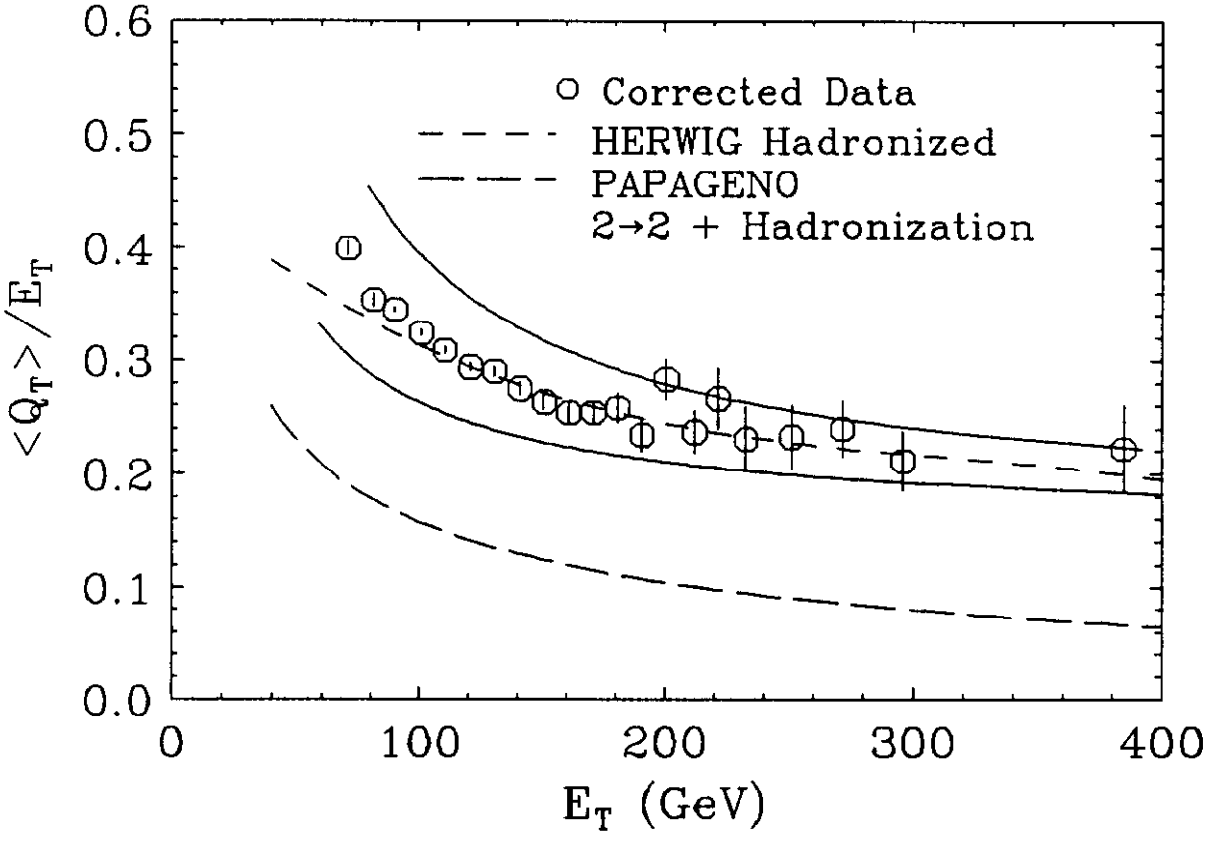

Figure 22: $< Q_T > / E_T$ vs. E_T for data compared to PAPAGENO $2 \Rightarrow 2$ + hadronization and compared to the HERWIG result from hadronized partons.

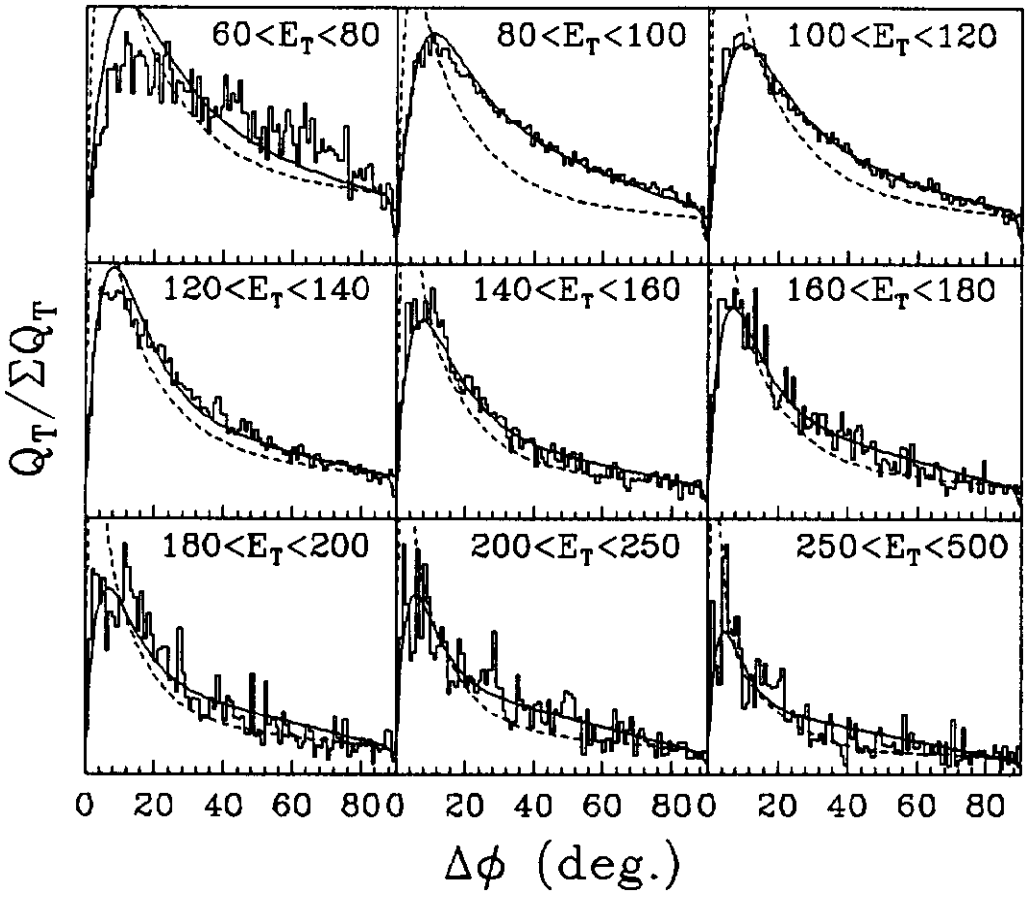

Figure 23: Histograms of fractional Q_T of each tower (averaged over events for each E_T interval) vs. $\Delta\phi$ between the tower and the thrust axis. Data are corrected for shape-changing detector effects and underlying event. Smoothed HERWIG (solid curve) and PAPAGENO (dashed curve) distributions are discussed in the text.